Drug Design, Development and Therapy Dovepress

Open Access Full Text Article ORIGINAL RESEARCH

Integrating Network Pharmacology and Metabolomics to Reveal the Immunomodulatory Mechanism of Ethnomedicine *Rodgersia sambucifolia* Hemsl

Jiayue Zhou[1,2], Yingxiang Wu[1,2], Zhiyan Lu[1,2], Yan Wang[1,2]

[1]Yunnan Provincial Key Laboratory of Entomological Biopharmaceutical R&D, Dali University, Dali, Yunnan Province, 671000, People's Republic of China; [2]National-Local Joint Engineering Research Center of Entomoceutics, Dali University, Dali, Yunnan Province, 671000, People's Republic of China

Correspondence: Yan Wang, Yunnan Provincial Key Laboratory of Entomological Biopharmaceutical R&D, Dali University, Dali, Yunnan Province, 671000, People's Republic of China, Tel +86 0872-2257401, Email jessica9428@sina.com

Purpose: *Rodgersia sambucifolia* Hemsl (also known as ***Yantuo***) is a traditional Chinese medicine commonly utilized as a medicinal herb with its rhizomes, mainly used to regulate the immune function of the human body. However, relatively few studies have investigated its active components and potential mechanisms of action in vivo.

Methods: First, the chemical composition in vitro was identified and analyzed using the UPLC-Q-TOF MS/MS technique. Cyclophosphamide (CTX) was then administered intraperitoneally to rats to establish an immunosuppression model. Physiological and biochemical parameters, organ indices, and histopathological findings were evaluated for efficacy. Subsequently, potential biomarkers in rat serum were identified using multivariate statistical analysis and enriched and topologized using online platforms such as MetaboAnalyst and KEGG to reveal the critical metabolic pathways and their roles in the immunomodulatory network. Finally, the integrated analysis of components in vivo and in vitro, along with metabolic pathways, was performed using network pharmacology and molecular docking technology to elucidate the mechanisms of their roles in organismal immunity.

Results: A total of 28 chemical components in vitro were identified, while pharmacodynamic experiments confirmed the immunomodulatory effects of ***Yantuo***, especially in the high-dose administration group. Metabolomics analysis showed that 37 potential immune-related biomarkers were identified in positive and negative ion modes, involving 16 metabolic pathways such as arginine biosynthesis, pyrimidine metabolism, and riboflavin metabolism. The results of network pharmacology and molecular docking indicated that ***Yantuo*** may affect 7-O-galloyl-catechin, Cynaroside, Quercetin-7-O-beta-D-glucopyranoside, and 1.6-bis-O-galloyl-beta-D-glucose through interactions with the immune system, with significant pathways of action including galactose metabolism, glycolysis/gluconeogenesis, pyrimidine metabolism, and riboflavin metabolism.

Conclusion: In our experiments, we confirmed the organismal modulatory effect of ***Yantuo*** on immunocompromised rats, clarified the key components, target proteins, and pathways of its possible action, and provided possibilities for follow-up studies.

Keywords: immunosuppression, *Yantuo*, metabolomics, network pharmacology, molecular docking

Introduction

Yantuo (*Rhizoma Rodgersiae*, RR) is the dried rhizome of *Rodgersia sambucifolia* Hemsl or *Rodgersia pinnata* Hemsl, belonging to the family *Saxifragaceae Juss*. It is primarily harvested in the provinces of Yunnan, Guizhou, Shanxi, and Sichuan[1] and is a traditional medicinal herb among the Bai, Lisu, and Miao ethnic groups.[2] Research has demonstrated that ***Yantuo*** exhibits a variety of pharmacological activities[3] and can be utilized for its anti-inflammatory properties and regulation of immune system functions.[4–11]Wu Changyue,[12] Lv Tao,[13] and other researchers have demonstrated that flavonoid extracts from ***Yantuo*** can improve biochemical indices and increase the expression levels of serum cytokines IgG and IgM, thereby enhancing the immune function of rats. This finding supports the notion that flavonoids boost

Received: 19 July 2024
Accepted: 3 October 2024
Published: 24 October 2024

Graphical Abstract

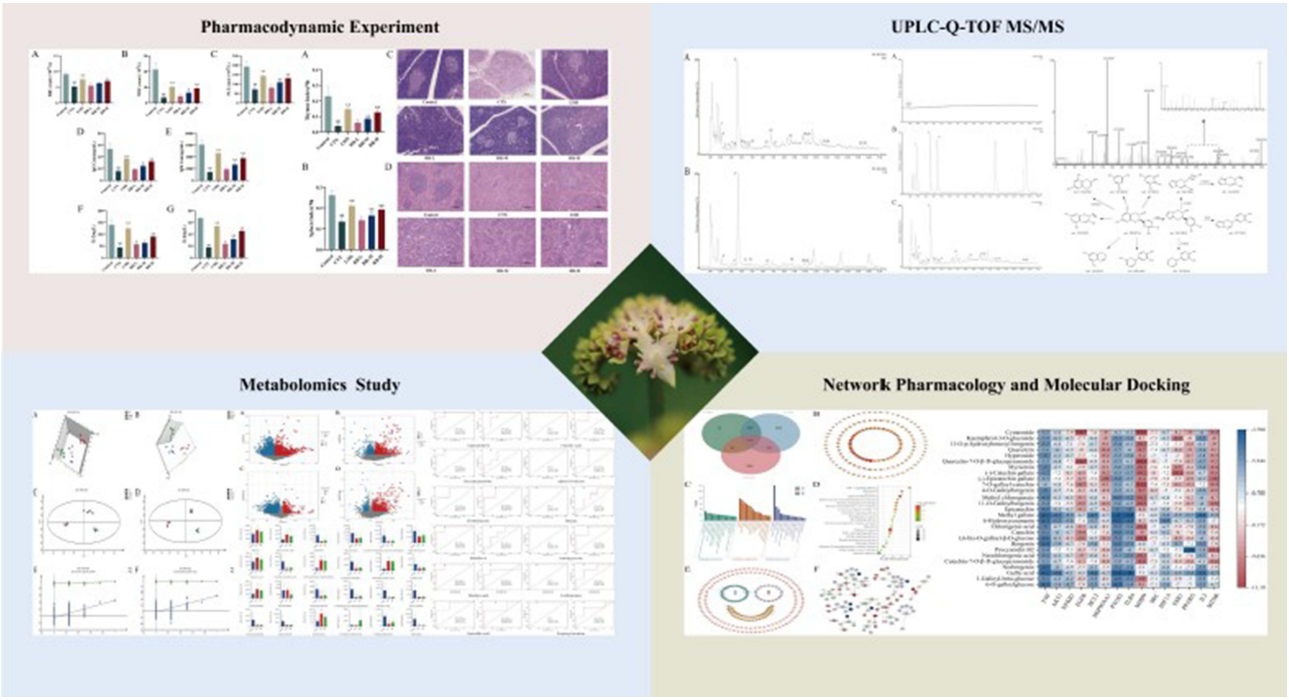

immune function by stimulating the body to secrete immune factors.[14–16] ***Yantuo***'s rhizome contains a variety of components. Currently, research on ***Yantuo*** mainly focuses on pharmacognosy, pharmacological effects, clinical applications, and extraction processes.[17–22] Although there have been some reports regarding its efficacy, systematic research is still lacking. The relationship between the material basis of pharmacodynamics, its mechanism of action, and its targets remains unclear, highlighting an urgent need for more comprehensive studies.

The body's immune system is influenced by multiple factors involving multi-targets and multi-pathways regulation and interactions among different aspects. Therefore, it is essential to conduct multidimensional and multilevel studies to leverage each other's strengths and uncover how drugs interact with the body's targets through diverse pathways, thus realizing the effect of immunomodulation.

The characterization of the multi-level and multi-system complex modes of action in traditional Chinese medicine (TCM) has always been a significant topic in modern TCM research.[23] ***Yantuo***, as traditional Chinese medicine, possesses the unique advantages of multi-targets and multi-pathways, and clarifying its material basis and targets is crucial for maximizing its therapeutic effects.[24] Fortunately, due to its holistic and systematic characteristics,[25] network pharmacology complements traditional Chinese medicine research and is frequently employed for pharmacodynamics-based substance investigations. Additionally, molecular docking technology significantly reduces the uncertainty in research by computer-simulating the interactions between small molecules and biological macromolecules, enabling virtual screening to identify active compounds.[26] Metabolomics, in contrast, takes endogenous small molecules (relative molecular mass less than 100) in organisms as the object of study. It amplifies the differences in metabolite levels by linking upstream genomic and downstream proteomic information[27] to detect subtle changes in the body better. It is commonly used to reveal the metabolic mechanisms of pathological conditions because its dynamic properties can be associated with specific diseases and physiological states.[28]

This study is the first to integrate components in vitro and differential metabolites in vivo for research, utilizing animal experiments and bioinformatics technology to construct a complex network of 'drug-components-differential metabolites-disease-pathways' to reveal the material basis of its medicinal effect, and to elucidate how the

ethnomedicinal drug ***Yantuo*** can modulate the body's immune response through multiple targets and pathways at a macroscopic level.

Materials and Methods

UPLC-Q-TOF-MS/MS Analysis

The chemical composition in vitro of RR was identified and analyzed using methods previously developed by our research group.[29] The three control substances–gallic acid, bergenin, and catechin (purity > 98%)were obtained from the National Institute for the Control of Pharmaceutical and Biological Products (NICPP, Beijing, China). Leucine enkephalin was purchased from Sigma Aldrich (St. Louis, MO, USA).

The TIC plots were collected in both positive and negative ion modes (as shown in Figure 1). The compounds' primary and secondary mass spectra were extracted using MassLynx 4.1 software and compared with the standards. The molecular formulas of the compounds corresponding to the chromatogram peaks were calculated through fitting, and the chemical structures and cleavage pathways were surmised with a margin of error of ±10 ppm. The results of the compound identification are presented in Table 1.

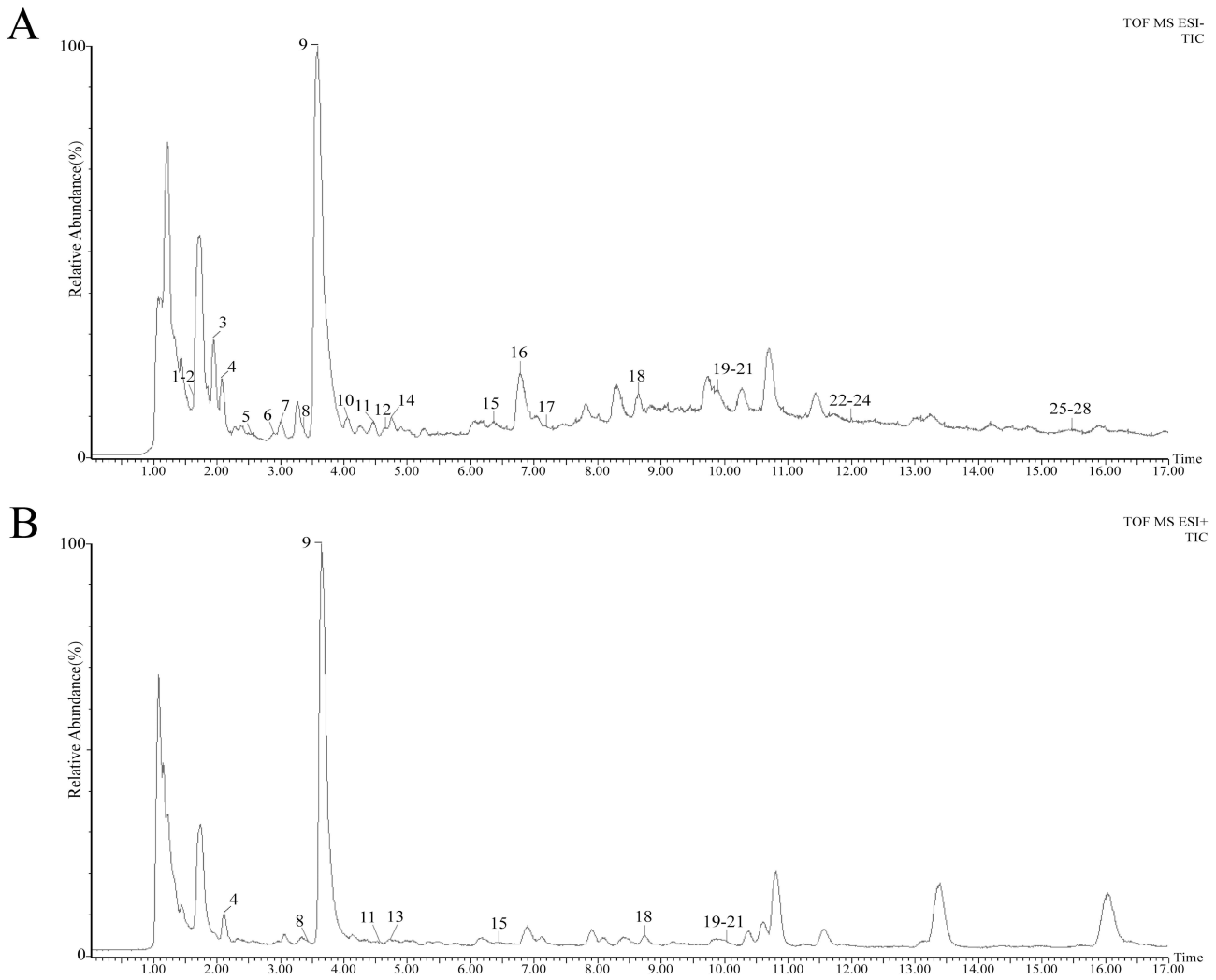

Figure 1 Total ion flow plots of RR samples in negative(**A**) and positive(**B**) ion modes.

Table 1 UPLC-Q-TOF-MS/MS Identification of RR Chemical Components in vitro

No.	tR(Time)	Negative Ion Mode		Positive Ion Mode		Identification	Formula	*m/z*	Ion Fragment $[M-H]^-$	Classification
		Indicated	ppm	Indicated	ppm					
1^-	1.62	331.0655	−3.02	-	-	6-O-galloyl glucose[30]	$C_{13}H_{16}O_{10}$	331.0665	331.0655 271.0468 211.0254 169.0138 151.0029 125.0243	A
2^-	1.62	331.0655	−3.02	-	-	1-Galloyl-beta-glucose[30]	$C_{13}H_{16}O_{10}$	331.0665	331.0655 271.0468 211.0254 169.0138 151.0029 125.0243	A
3*	1.95	169.0141	2.37	-	-	Gallic acid[31]	$C_7H_6O_5$	169.0137	169.0141 151.0209 125.0241 107.0137 81.0349 79.0184 69.0342	A
4^-	2.08	313.0537	−7.35	315.0717	0.32	Norbergenin[32]	$C_{13}H_{14}O_9$	313.056	313.0537 235.0202 193.0137 165.0194 137.0259	B
5^-	2.55	451.1195	−9.98	-	-	Catechin7-O-β-D-glucopyranoside[31]	$C_{21}H_{24}O_{11}$	451.1240	451.1185 289.0704 245.0801 192.0049 169.0137 137.0236 125.0241 109.0293 96.9602	C
6^-	2.89	489.1239	−1.02	-	-	11-β-D-glucopyranosyl bergenin[32]	$C_{20}H_{26}O_{14}$	489.1244	489.1239 313.0594 312.0489 327.0643 249.0408 207.0298 192.0062	B
7^-	3.02	353.0880	1.98	-	-	Neochlorogenic acid[31]	$C_{16}H_{18}O_9$	353.0873	353.0880 191.0564 179.0350 161.0240 135.0450	D
8^-	3.35	577.1346	0.00	579.1520	2.94	Procyanidin B2[32]	$C_{30}H_{26}O_{12}$	577.1346	577.1346 451.0896 425.0834 407.0789 289.0698 245.0813 205.0491 161.0238 143.0710 137.0243 125.0242	C

(*Continued*)

Table 1 (Continued).

No.	tR(Time)	Negative Ion Mode		Positive Ion Mode		Identification	Formula	*m/z*	Ion Fragment $[M-H]^-$	Classification
		Indicated	ppm	Indicated	ppm					
9*	3.59	327.0720	1.22	329.0870	−0.91	Bergenin[31]	$C_{14}H_{16}O_9$	327.0716	327.0720 312.0475 249.0398 234.0168 207.0302 192.0076	B
10^-	4.06	483.0760	−3.11	-	-	1,6-bis-O-galloyl-beta-D-glucose[30]	$C_{20}H_{20}O_{14}$	483.0775	483.0760 331.0668 313.0538 271.0458 169.0139 211.0242 125.0244	A
11*	4.47	289.0716	1.38	291.0864	−1.72	Catechin[33]	$C_{15}H_{14}O_6$	289.0712	289.0716 245.0831 227.0699 205.0503 203.0697 187.0393 179.0341 161.0237 151.0394 137.0246 125.0241 123.0447 109.0295	C
12^-	4.64	353.0877	1.13	-	-	Chlorogenic acid[31]	$C_{16}H_{18}O_9$	353.0873	353.0877 191.0554 137.0261 135.0444 127.0293	D
13^-	4.71	-	-	163.0386	−5.52	6-Hydroxycoumarin[34]	$C_9H_6O_3$	163.0395	163.0386 145.0281 135.0435 131.0495 117.0341 107.0492	B
14^-	4.75	183.0288	−2.73	-	-	Methyl gallate[31]	$C_8H_8O_5$	183.0293	183.0288 177.0176 169.0140 167.0344 161.0239 151.0400 139.0381 125.0242 124.0167 95.0464 61.9896	E
15^-	6.36	289.0703	−3.11	291.0870	0.34	Epicatechin[33]	$C_{15}H_{14}O_6$	289.0712	289.0703 245.0806 227.0699 203.0697 187.0393 179.0338 151.0396 137.0244 109.0290 169.0137 125.0241	C

(*Continued*)

Table 1 (Continued).

No.	tR(Time)	Negative Ion Mode		Positive Ion Mode		Identification	Formula	*m/z*	Ion Fragment $[M-H]^-$	Classification
		Indicated	ppm	Indicated	ppm					
16^-	6.77	479.0821	−1.04	-	-	11-O-Galloyl-bergenin[31]	$C_{21}H_{20}O_{13}$	479.0826	479.0821 327.0727 312.0499 249.0401 207.0287 193.0132 169.0144 125.0245	B
17^-	7.17	367.1038	2.45	-	-	Methyl chlorogenate[35]	$C_{17}H_{20}O_9$	367.1029	367.1038 191.0544 179.0339 173.0599 134.0369 93.0357 125.0242 169.0136	E
18^-	8.64	479.0829	0.63	481.0987	1.04	4-O-Galloyl bergenin[31]	$C_{21}H_{20}O_{13}$	479.0826	479.0829 327.0682 313.0592 249.0391 207.0296 193.0140 169.0140	B
19^-	9.89	441.0806	−3.63	443.0967	−2.48	7-O-galloyl-catechin[31]	$C_{22}H_{18}O_{10}$	441.0822	441.0806 289.0706 245.0448 169.0141 137.0242 169.0141 125.0243	C
20^-	9.89	441.0806	−3.63	443.0967	−2.48	(-)-Epicatechin gallate[35]	$C_{22}H_{18}O_{10}$	441.0822	441.0806 331.0569 289.0706 245.0448 205.0490 179.0346 169.0141 125.0243	E
21^-	9.89	441.0806	−3.63	443.0967	−2.48	(-)-Catechin gallate[35]	$C_{22}H_{18}O_{10}$	441.0822	441.0806 331.0569 289.0706 245.0448 205.0490 179.0346 169.0141 125.0243	E
22^-	11.92	463.0837	−8.64	-	-	Myricitrin[36]	$C_{21}H_{20}O_{12}$	463.0877	463.0837 287.0557 271.0249 300.0255 315.0381 169.0143 125.0245 151.0400	C

(*Continued*)

Table 1 (Continued).

No.	tR(Time)	Negative Ion Mode		Positive Ion Mode		Identification	Formula	*m/z*	Ion Fragment [M-H]⁻	Classification
		Indicated	ppm	Indicated	ppm					
23⁻	11.92	463.0837	−8.64	-	-	Quercetin-7-O-β-D-glucopyranoside[30]	$C_{21}H_{20}O_{12}$	463.0877	463.0837 303.0504 301.0337 300.0255 271.0248 255.0298 178.9977 151.0037	C
24⁻	11.92	463.0837	−8.64	-	-	Hyperoside[31]	$C_{21}H_{20}O_{12}$	463.0877	463.0837 303.0504 301.0337 300.0255 271.0249 179.0348 161.0247 151.0400	C
25⁻	15.47	447.0936	2.01	-	-	Quercitrin[33]	$C_{21}H_{20}O_{11}$	447.0927	447.0936 301.0332 300.0272 271.0241 151.0394	C
26⁻	15.47	447.0936	2.01	-	-	11-O-p-hydroxybenzoyl bergenin[31]	$C_{21}H_{20}O_{11}$	447.0927	447.0884 234.0176 207.0269 192.0063 137.0202 407.0738 395.0750 303.0502 287.0553 271.0236 243.0294 169.0143 125.0242	B
27⁻	15.47	447.0936	2.01	-	-	Kaempferol 3-O-glucoside[37]	$C_{21}H_{20}O_{11}$	447.0927	447.0936 227.0345 255.0287 285.0402 151.0394 125.0244 169.0142 243.0303	C
28⁻	15.47	447.0915	−2.68	-	-	Cynaroside[38]	$C_{21}H_{20}O_{11}$	447.0927	447.0915 285.0393 255.0352 227.0351 151.0401 133.0305	C

Notes:*Represents for standard comparisons,⁻represents potential new compounds; A: polyphenols; B: coumarin analogues; C: flavonoids; D: phenylpropanoids; E: Esters.

Animal Experiments

Herbs and Reagents

The herbs used in this study were identified by Dr. Dequan Zhang of Dali University and preserved in Dr. Yan Wang's research group (Voucher Number: DLUWYXN14-20).[39] The herbs were macerated in 60% methanol overnight, extracted via reflux, and then concentrated through evaporation. The lyophilized powder was prepared from the concentrate and stored for future use. Methanol and chromatographic-grade solvents were purchased from Scientific

Sciences (Loughborough, UK). The internal standard, 2-chloro-L-phenylalanine (purity > 98%), was obtained from Aladdin (Shanghai, China). Formic acid was purchased from TCI (Shanghai, China), and formate was sourced from Aldrich Aldridge (Shanghai, China). Deionized water was produced using the Milli-Q system (Millipore, Billerica, MA, USA).

Grouping of Experimental Animals and Administration of Drugs

Thirty-six male SD rats, aged 6–7 weeks, were purchased from Spearfish (Beijing) Biotechnology Co. Ltd (Animal License No.: SCXK (Beijing) 2019–0010). The experimental animals were kept in an environment with a temperature of 22±4°C and relative humidity of 55±15%, during which they were allowed to drink freely. After one week of acclimatization, the animals were randomly divided into six groups based on body weight, with six animals in each group (n=6). The groups included a blank group, a model group (CTX group), three RR dosage administration groups (low, medium, and high dosages of 0.3 g/kg/d, 0.6 g/kg/d, and 1.2 g/kg/d, respectively), and a levamisole positive control group (LMS group). Disease modeling was established by intraperitoneal injection of CTX (purchased from Baxter Oncology GmbH) into the model group, the three dosage administration groups, and the positive control group on days 1–3, 4–5, 9, and 12 of the experiment, respectively. For the first three days, a dosage of 40 mg/kg/d was administered, followed by 20 mg/kg/d for the remainder of the study. Meanwhile, the RR suspension was prepared by dissolving 0.5% carboxymethyl cellulose sodium (CMC-Na). The treatment of rats in the RR group lasted for 2 weeks and was administered via gavage based on the body weight of each rat. To control for external factors, rats in the control, CTX, and LMS groups received the same volume of CMC-Na (LMS was purchased from Guangdong Nan Guo Pharmaceutical Co., Ltd.) via gavage as the rats in the RR group. An equal volume of saline was used for the blank control group during this period (as shown in Figure 2). The experimental protocol was approved by the Laboratory Animal Welfare Ethics Committee of Dali University (Ethics No. 2022-P2-91) in accordance with the guidelines set forth by the Animal Welfare Council of China.

Sample Collection and Processing

Twenty-four hours after the final administration, blood was collected from the tail veins of the rats to assess whole blood indices, including red blood cells, white blood cells, and platelets. The results are presented in Figure 3A–C. The rats were anesthetized with isoflurane, and blood was collected from the abdominal aorta. The thymus and spleen tissues were excised for weighing and calculation, followed by the rats'execution. The organ indices are displayed in Figure 4A and B. Tissues were fixed in a 4% paraformaldehyde solution and stained with hematoxylin and eosin (HE) for histopathological analysis, as shown in Figure 4C and D. Blood samples were allowed to stand at room temperature for one hour before being centrifuged at 3000 r/min for 10 min at 4 °C. Serum was then prepared and stored at −80 °C for subsequent metabolomics analysis. Immunoglobulin (IgG, IgM) and serum cytokine (IL-2, IL-6) levels were quantified using enzyme-linked immunosorbent assay (ELISA), with results illustrated in Figure 3D–G. The kits used for these assays were obtained from Nanjing Jianjian Bioengineering Institute.

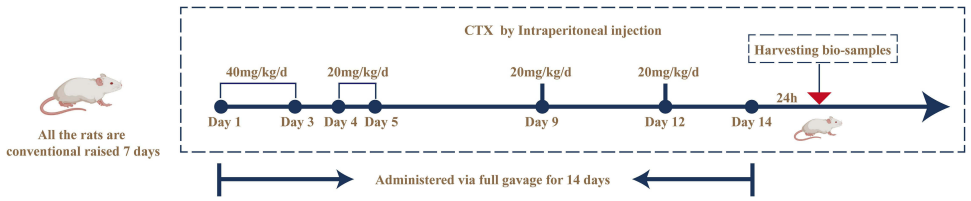

Figure 2 Animal experiment flow chart.

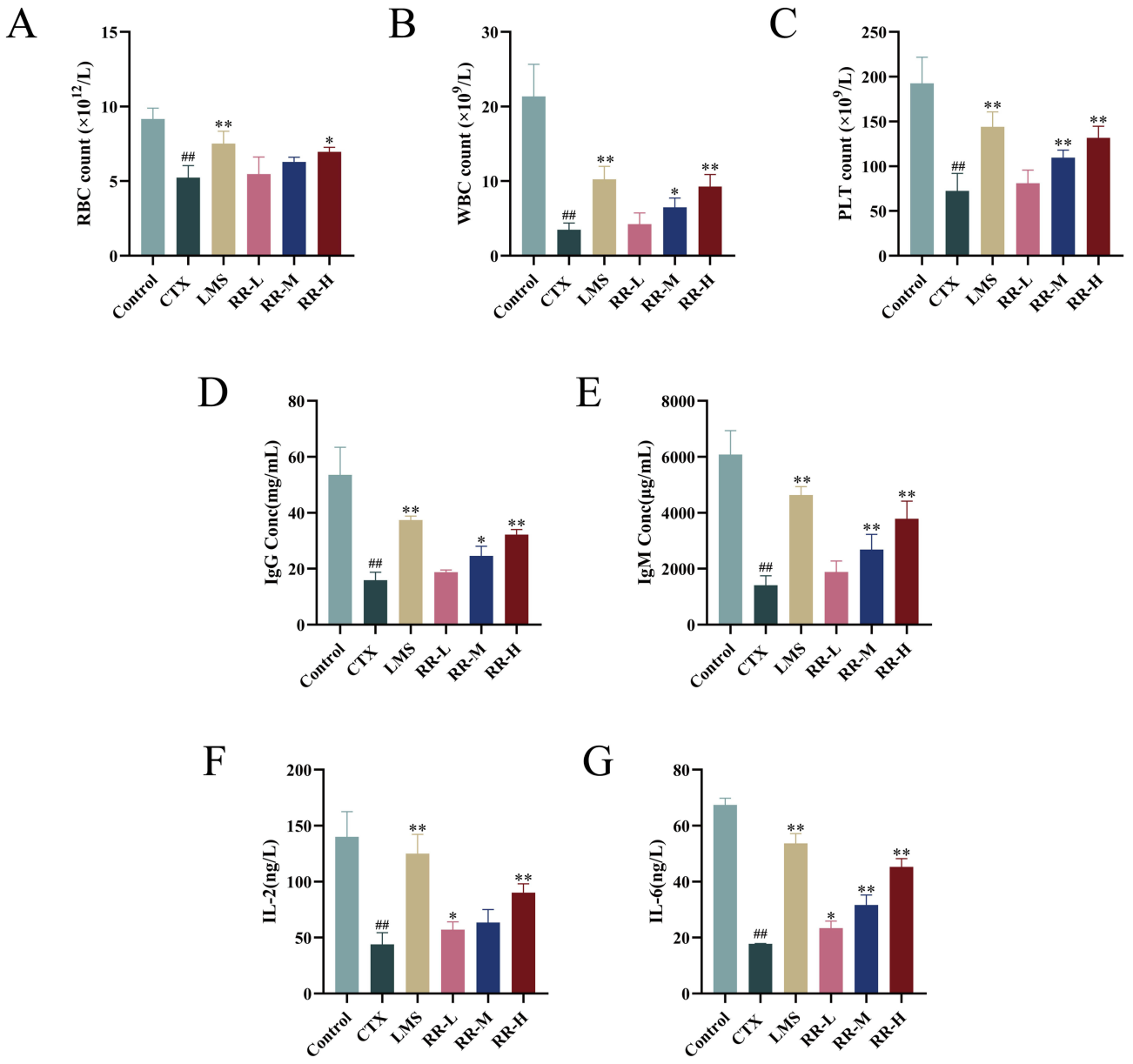

Figure 3 Effect of RR extract on hematological indices in immunosuppressed model rats. (**A**): RBC; (**B**): WBC; (**C**): PLT; (**D**): IgG; (**E**): IgM; (**F**): IL-2; (**G**): IL-6. $^{\#\#}P < 0.01$, vs the control group;$^{*}P < 0.05$, $^{**}P < 0.01$, vs the model group.

Metabolomics Analysis

Sample Preparation

The serum samples were thawed at 4 °C and vortexed for 1 min. An appropriate sample volume was transferred to a 2 mL centrifuge tube, and the proteins were precipitated by adding 400 μL of a methanol solution (stored at −20 °C) and vortexing for 1 min. The mixture was then centrifuged at 12,000 rpm for 10 min at 4 °C, and the supernatant was transferred to a new 2 mL tube for concentration and drying. Accurately add 150 μL of a 2-chloro-L-phenylalanine solution prepared with 80% methanol and water (stored at 4 °C) to re-dissolve the sample. The supernatant was filtered through a membrane with a pore size of 0.22 μm and was subsequently used for LC-MS analysis.[40]

LC-MS Analytical Conditions

The LC analysis was performed on a Vanquish UHPLC System (Thermo Fisher Scientific, USA). Chromatography was carried out with an ACQUITY UPLC®HSS T3 (150×2.1 mm, 1.8 μm) (Waters, Milford, MA, USA). The column was maintained at

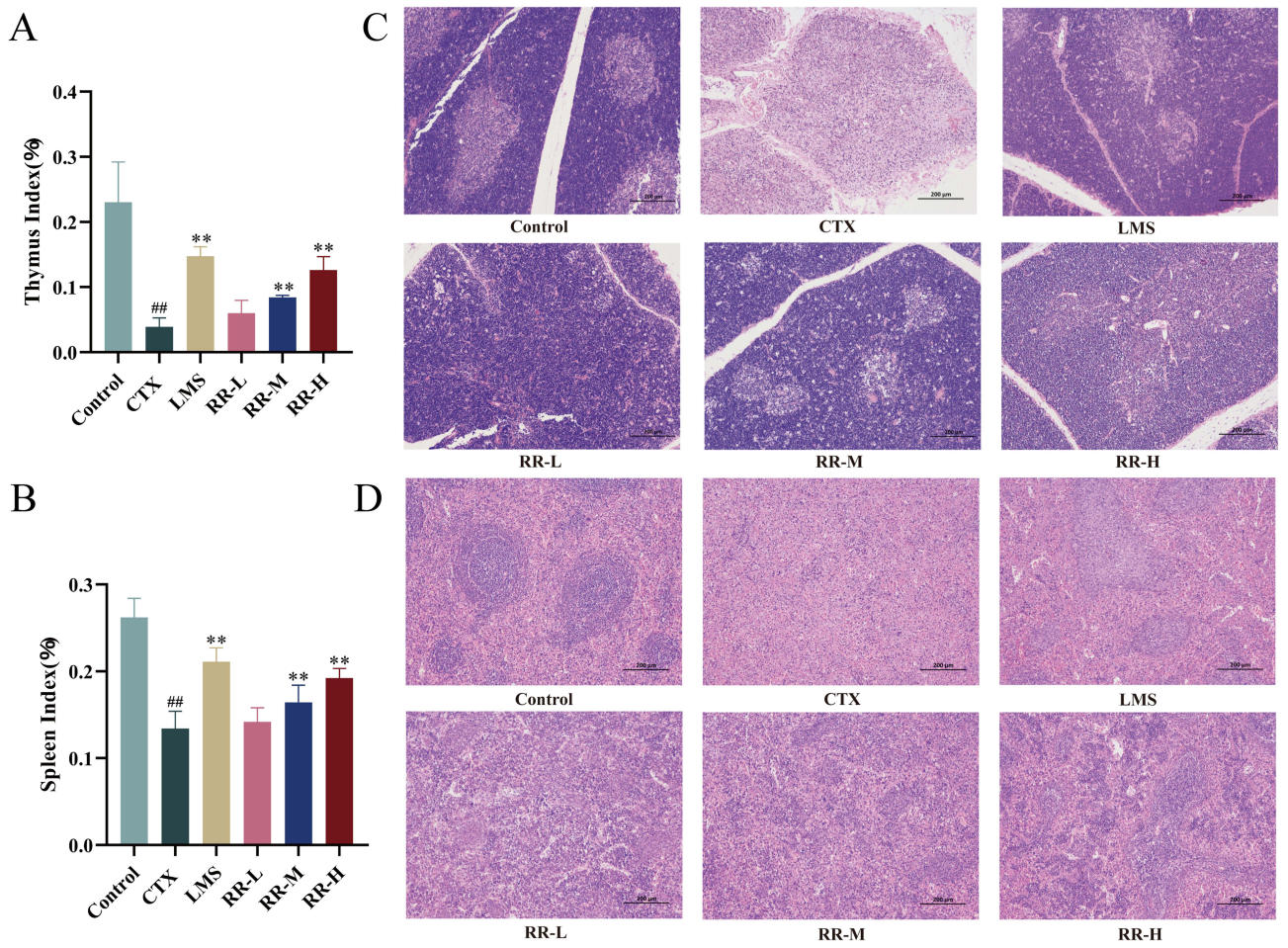

Figure 4 Effect of RR extract on organ and histopathology in immunosuppressed model rats. (**A**): thymus index; (**B**): Spleen index; (**C**): Thymus HE staining results; (**D**): Spleen HE staining results.$^{\#\#}P < 0.01$, vs the control group; $^{**}P < 0.01$, vs the model group.

40 °C. The flow rate and injection volume were set at 0.25 mL/min and two μL, respectively. For LC-ESI (+)-MS analysis, the mobile phases consisted of (C) 0.1% formic acid in acetonitrile (v/v) and (D) 0.1% formic acid in water (v/v). Separation was conducted under the following gradient: 0~1 min, 2% C; 1~9 min, 2%~50% C; 9~12 min, 50%~98% C; 12~13.5 min, 98% C; 13.5~14 min, 98%~2% C; 14~20 min, 2% C. For LC-ESI (-)-MS analysis, the analytes were carried out with (A) acetonitrile and (B) ammonium formate (5 mm). Separation was conducted under the following gradient: 0~1 min, 2%A; 1~9 min, 2% ~50%A; 9~12 min, 50%~98%A; 12~13.5 min, 98%A; 13.5~14 min, 98%~2%A; 14~17 min, 2%A.[41]

Mass spectrometric detection of metabolites was performed on Orbitrap Exploris 120 (Thermo. Fisher Scientific, USA) with ESI ion source. Simultaneous MS1 and MS/MS (Full MS-ddMS2 mode, data-dependent MS/MS) acquisition was used. The parameters were as follows: sheath gas pressure, 30 arb; aux gas flow, ten arb; spray voltage, 3.50 kV and −2.50 kV for ESI(+) and ESI(-), respectively; capillary temperature, 325 °C; MS1 range, m/z 100–1000; MS1 resolving power, 60000 FWHM; number of data dependant scans per cycle, 4; MS/MS resolving power, 15000 FWHM; normalized collision energy, 30%; dynamic exclusion time, automatic.[42]

Non-Targeted Metabolomics Analysis

Raw mass spectrum files were converted to mzXML file format using the MSConvert tool in the Proteowizard package (v3.0.8789).[43] Peak detection, peak filtering, and peak alignment processes were performed using the RXCMS software package[44] to obtain a list of quantitative substances. Public databases HMDB,[45] MassBank,[46] LipidMaps,[47] Mzclound,[48] KEGG,[49] and self-built libraries were used for substance identification.

Screening for Identification of Differential Metabolites

Subsequently, the identification results were imported into SIMCA software for multivariate statistical analysis, including principal component analysis (PCA) and orthogonal partial least squares discriminant analysis (OPLS-DA), and the results are shown in Figure 5. Data can be corrected for signals from QC samples to eliminate systematic errors and enhance data reliability. To prevent overfitting of the model, we used a 200-times replacement test to verify the reliability of the model results. In this study, metabolites with a variable of predicted importance (VIP) >1 and a fold reduction in difference (FC) >1 or FC <0.5 in the OPLS-DA analysis were defined as significantly different metabolites using the Student's *t*-test, requiring P <0.05. A total of 37 different metabolites were identified in the positive-negative ion model, as shown in Table 2. The two-by-two comparisons of different metabolite results were visualized using volcano diagrams for the visualization and analysis (Figure 6). Also, the accuracy of potential biomarkers was verified using subject work characterization (ROC) curves(Figure 7).

Differential metabolites pathway analysis (Figure 8) and topology analysis (Table 3) were performed using the MetaboAnalyst website to establish the potential pathways closely associated with the biomarkers, and the pathway regulatory network results are shown in Figure 9.

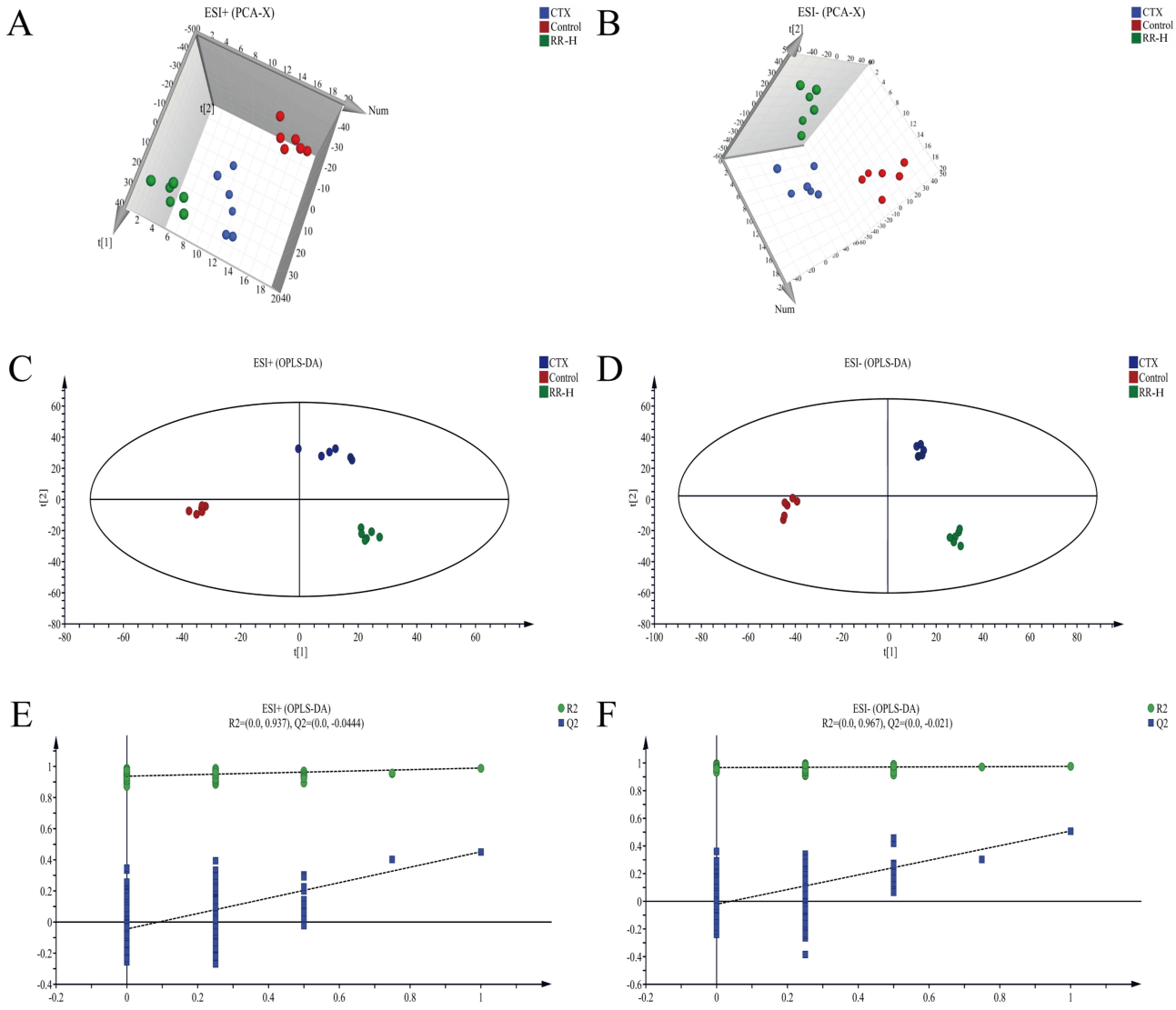

Figure 5 Multivariate statistical analysis of rat serum in high dose group in positive and negative ion mode.(**A**): PCA analysis in positive ion mode;(**B**): PCA analysis in negative ion mode; (**C**): OPLS-DA analysis in positive ion mode; (**D**): OPLS-DA analysis in negative ion mode; (**E**): Results of the OPLS-DA substitution test in positive ion mode; (**F**): Results of the OPLS-DA substitution test in negative ion mode.

Table 2 Identified Different Metabolites Among Groups in Serum in Positive and Negative Ion Mode

No.	Metabolite Name	*m/z*	t_R /min	Molecular Formula	Measured Value	ppm	CTX vs Control			RR vs CTX			Ion mode
							VIP	FC	Trend	VIP	FC	Trend	
1	1-Linoleoylglycerophosphocholine	520.3476	0.52	$C_{26}H_{51}NO_7P$	520.3476	14.0291	1.41	0.05	$\downarrow^{\#\#}$	1.55	2.03	↑	Pos
2	Fumaric acid	115.0042	1.28	$C_4H_4O_4$	115.0042	4.139	1.06	1.97	$\uparrow^{\#\#}$	1.91	0.84	↓	Neg
3	L-Glutamic acid	146.0465	1.31	$C_5H_9NO_4$	146.0465	3.9439	1.57	0.01	$\downarrow^{\#\#}$	1.04	3.93	↑	Neg
4	Betaine	118.0865	1.47	$C_5H_{11}NO_2$	118.0865	1.8969	1.23	2.76	$\downarrow^{\#}$	1.6	0.88	↓	Pos
5	gamma-Glutamylcysteine	248.9615	1.47	$C_8H_{14}N_2O_5S$	248.9615	5.2566	1.83	1.45	↑	1.13	0.09	↓	Neg
6	Dimethylglycine	104.0705	1.55	$C_4H_9NO_2$	104.0705	−0.7303	1.82	0.25	↓	1.08	0.85	↓	Pos
7	Pseudouridine	243.0637	1.67	$C_9H_{12}N_2O_6$	243.0637	5.9239	1.44	0.02	↓	1.24	0.43	↓**	Neg
8	Creatinine	112.9861	1.91	$C_4H_7N_3O$	112.9861	14.9973	1.76	1.42	↑	1.72	0.48	↓	Neg
9	Uracil	111.0199	2.42	$C_4H_4N_2O_2$	111.0199	−1.0809	1.74	0.04	$\downarrow^{\#\#}$	1.18	0.94	↓	Neg
10	Indolepyruvate	204.063	2.98	$C_{11}H_9NO_3$	204.063	−2.3463	1.98	0	$\downarrow^{\#}$	1.26	0.47	↓	Pos
11	Homocitrulline	190.1079	2.79	$C_7H_{15}N_3O_3$	190.1079	0.8823	1.34	0.02	$\downarrow^{\#}$	1.63	0.85	↓	Pos
12	Homovanillic acid	182.9851	3.28	$C_9H_{10}O_4$	182.9851	0.5465	1.23	4.05	$\uparrow^{\#}$	1.81	0.81	↓	Pos
13	Propionylcarnitine	218.1389	4.1	$C_{10}H_{19}NO_4$	218.1389	0.9898	1.52	0.07	$\downarrow^{\#\#}$	1.41	1.39	↑	Pos
14	L-Kynurenine	209.0926	5.33	$C_{10}H_{12}N_2O_3$	209.0926	−0.2489	1.34	0.28	$\downarrow^{\#}$	1.69	1.18	↑	Pos
15	1-Methyladenosine	282.1193	5.37	$C_{11}H_{15}N_5O_4$	282.1193	−0.8004	1.35	0.33	$\downarrow^{\#\#}$	1.99	1.67	↑*	Pos
16	Acetylcholine	146.1176	5.97	$C_7H_{16}NO_2$	146.1176	0.0035	1.39	0.48	↓	1.77	1	↑	Pos
17	Alpha-D-Glucose	161.0433	6.16	$C_6H_{12}O_6$	161.0433	−10.6183	1.17	0.36	$\downarrow^{\#}$	1.43	1.21	↑	Neg
18	Thiabendazole	202.0449	6.54	$C_{10}H_7N_3S$	202.0449	0.8819	1.85	1.81	↑	2.01	0.93	↓	Pos
19	Quinaldic acid	174.055	7.12	$C_{10}H_7NO_2$	174.055	−0.0829	1.75	0.15	↓	2.54	1.1	↑	Pos
20	Sakuranetin	285.08	7.24	$C_{16}H_{14}O5$	285.08	11.0581	1.77	0	↓	2.46	6.36	↑*	Neg
21	Docosahexaenoic acid	328.1969	7.5	$C_{22}H_{32}O_2$	328.1969	−6.8308	1.71	0.39	$\downarrow^{\#\#}$	1.05	0.96	↓	Pos
22	25-Hydroxycholesterol	401.0867	9.03	$C_{27}H_{46}O_2$	401.0867	−1.8413	1.55	0.78	↓	2.3	6.52	↑*	Neg

23	Maslinic acid	472.2511	9.89	$C_{30}H_{48}O_4$	472.242	1.5416	1.06	0.06	$\downarrow^{\#}$	1.48	3.04	↑	Neg
24	Glycochenodeoxycholic acid	449.308	9.97	$C_{26}H_{43}NO_5$	449.308	−2.91	1.28	0.04	↓	1.84	2.37	↑	Neg
25	Quinic acid	164.1072	10.29	$C_{10}H_{13}NO$	164.1072	1.365	1.3	0.33	$\downarrow^{\#}$	1.07	1.43	↑	Pos
26	Pyrrole-2-carboxylic acid	111.0207	11.22	$C_5H_5NO_2$	111.0207	4.1363	1.67	0.05	$\downarrow^{\#}$	1.87	1.11	↑	Pos
27	Chenodeoxycholic acid	391.2862	12.12	$C_{24}H_{40}O_4$	391.2862	1.9832	1.4	0.24	$\downarrow^{\#\#}$	1.69	1.86	↑	Neg
28	Fenfluramine	232.1331	12.23	$C_{12}H_{16}F_3N$	232.1331	−0.089	1.31	2.21	$\uparrow^{\#\#}$	1.59	0.76	↓	Pos
29	Deoxyuridine	228.1954	12.37	$C_9H_{12}N_2O_5$	228.1954	−1.3336	1.68	0.42	$\downarrow^{\#}$	1.35	1.15	↑	Pos
30	Ergocalciferol	396.23	12.43	$C_{28}H_{44}O$	396.2214	8.1516	1.42	0.32	↓	1.02	1.17	↑	Neg
31	Thymidine	223.0291	12.57	$C_{10}H_{14}N_2O_5$	223.0291	5.4146	1.61	0.09	$\downarrow^{\#\#}$	1.41	1.79	↑	Neg
32	Hexadecanedioate	285.2071	12.8	$C_{16}H_{30}O_4$	285.2071	−0.0841	1.52	0.13	$\downarrow^{\#}$	1.23	1.4	↑	Neg
33	1-palmitoyl-dihydroxyacetone-phosphate	407.2195	13.03	$C_{19}H_{37}O_7P$	407.2195	−2.269	1.27	0.03	$\downarrow^{\#}$	1.03	1.89	↑	Neg
34	Docosatetraenoyl Ethanolamide	376.3127	13.18	$C_{24}H_{41}NO_2$	376.3127	−13.6007	1.22	0.01	$\downarrow^{\#\#}$	1.72	2.63	↑	Pos
35	Riboflavin	376.2581	13.18	$C_{17}H_{20}N_4O_6$	376.2581	−2.6885	1.45	0.32	$\downarrow^{\#}$	1.46	1.55	↑	Pos
36	Methylmalonic acid	116.9288	13.22	$C_4H_6O_4$	116.9288	12.2607	1.68	0.04	↓	1.14	0.87	↓*	Neg
37	11-Dehydrocorticosterone	325.1843	13.33	$C_{21}H_{28}O_4$	325.1843	11.9624	1.83	0.52	↓	1. 99	0.11	↓	Neg

Notes: $^{\#}P<0.05$, $^{\#\#}P<0.01$ compared with Control group; $^{*}P<0.05$, $^{**}P<0.01$ compared with CTX group.

https://doi.org/10.2147/DDDT.S479341

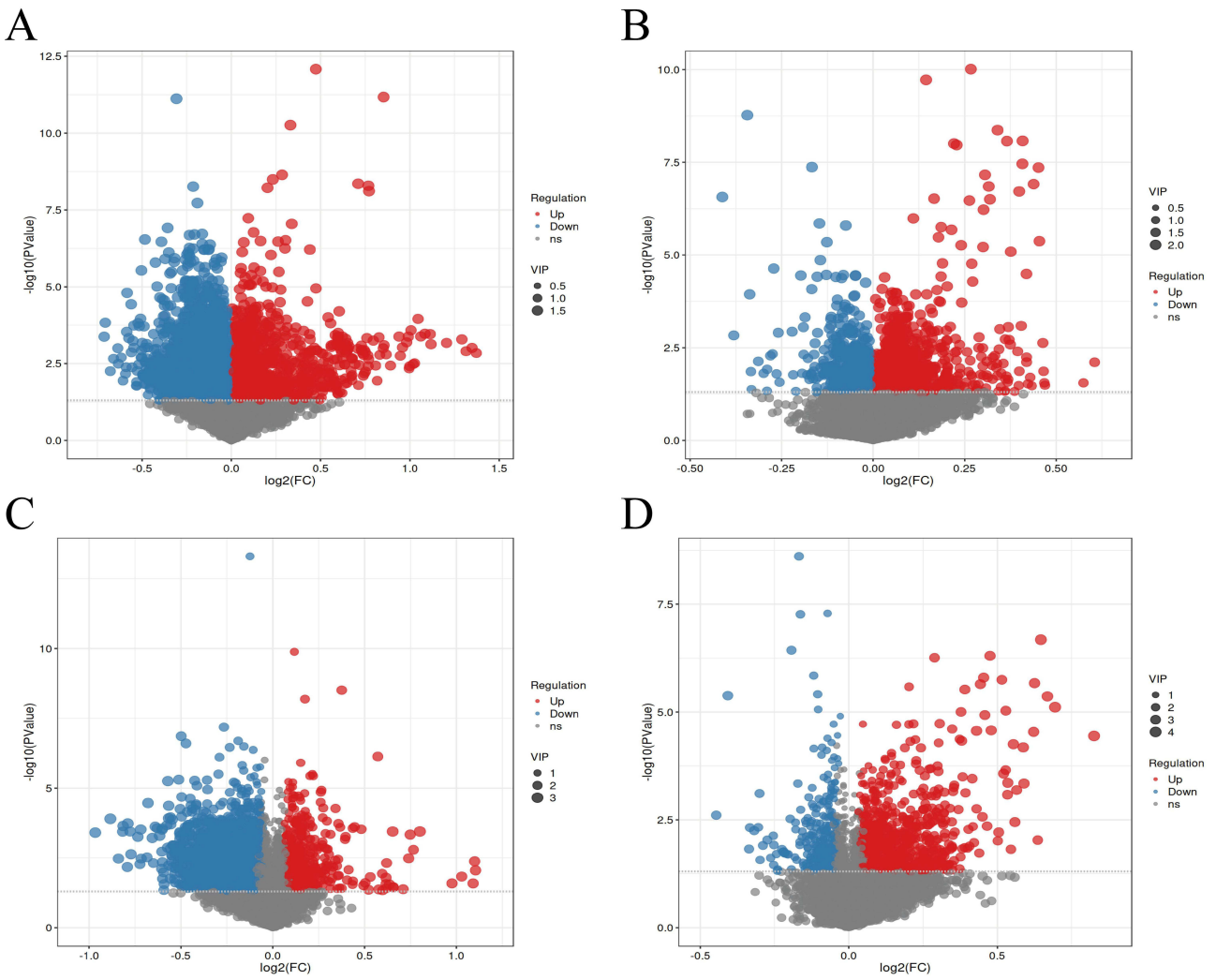

Figure 6 Differential metabolite identification volcano plots. (**A**): CTX vs Control; (**B**): RR vs CTX; (**C**): CTX vs Control; (**D**): RR vs CTX; (**A**) and (**B**) are in positive ion mode; (**C**) and (**D**) are in negative ion mode.

Network Pharmacology Analysis

To elucidate the role of extracorporeal substances in diseases, we constructed a "drug-components in vitro-different metabolites-disease-pathways" network with the help of Cytoscape 3.9.1(Figure 10), which was divided into the following five steps: (1) We utilized websites such as Swiss Target Prediction, BATMAN-TCM, and SuperPred to gather targets of compounds identified in vitro by RR and targets of differential metabolites identified in vivo. Additionally, we conducted searches using keywords such as "immunosuppression" in the DisGeNET, GeneCards, TTD, and OMIM databases to collect disease targets.(2) After merging and de-duplicating the targets, we obtained intersecting targets with the help of the Jvenn online platform;(3) The intersecting targets were imported into the String database, drew the PPI network, and the network was beautified with the help of Cytoscape software. At the same time, the top 15 targets were ranked as the core targets with the degree value as the screening criteria; (4) GO analysis and KEGG analysis of intersecting targets were performed with the help of David's database, and FDR < 0.01 and count values were used as criteria. The top 15 and top 20 results were visualized and analyzed separately;(5) Integrate and analyze the results to build a "drug-components in vitro-differential metabolites-disease-pathways" network.

Molecular Docking

The 2D structures of compounds obtained from the PubChem database were energetically optimized using chem3D software and then imported into the autodock tools for pre-processing. Suitable protein structures were selected from the UniProt

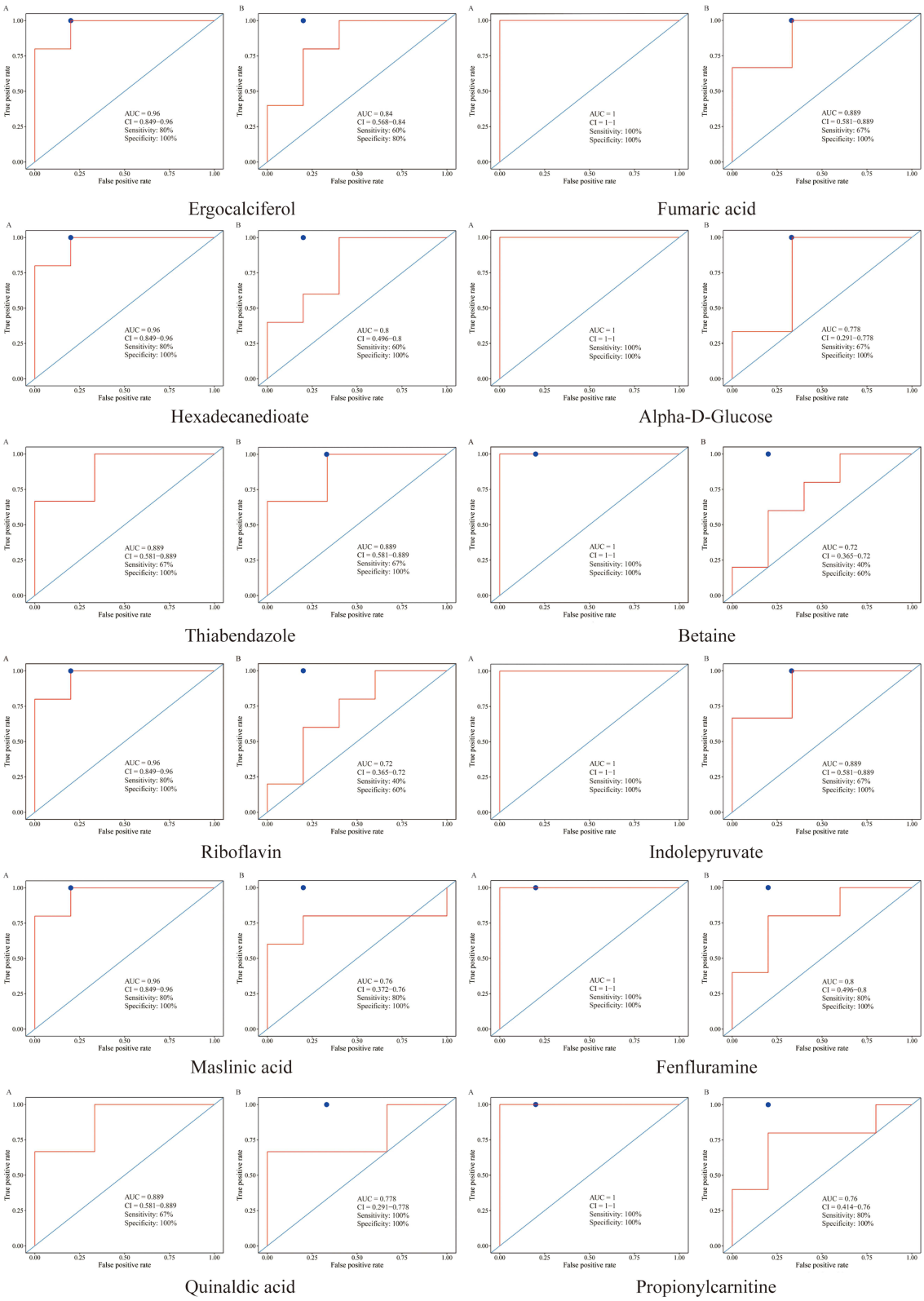

Figure 7 ROC plots for vital differential metabolites. The horizontal axis represents the false positive rate, while the vertical axis indicates the true positive rate. The red curve illustrates the actual performance, the blue curve serves as the baseline, and the blue dots denote the cutoff values. (**A**): CTX vs Control; (**B**): RR vs CTX.

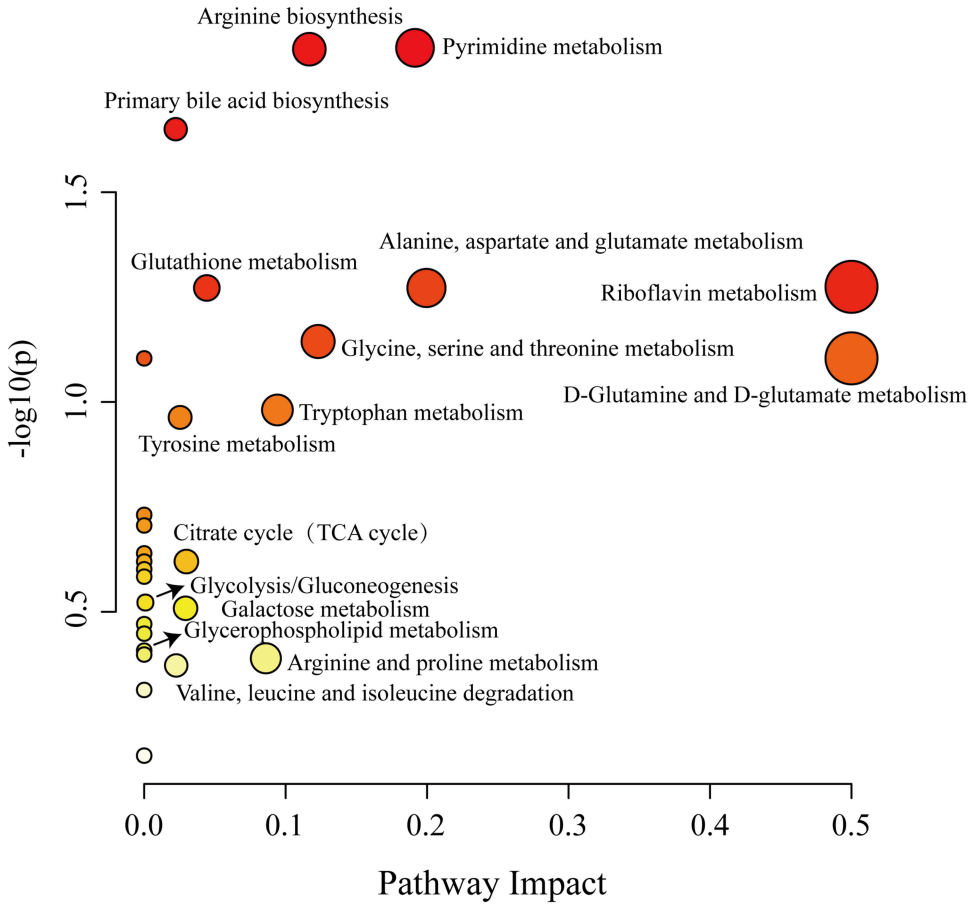

Figure 8 Bubble plots for pathways analysis of differential metabolites. Bubble size correlates with the number of differential metabolites enriched in the pathway; the more significant the bubble, the higher the number enriched; bubble color shade correlates with -$\log_{10}$(***P***); the darker the color, the smaller the p-value.

database and pre-processed using Pymol and autodock tools. The 15 target proteins identified by screening in Table 4 were batch-docked with 28 small molecule compounds using autodock vina software to calculate the binding energy, and the results are shown in Table 5. Intermolecular forces in the complexes were evaluated, and the four conformations with the lowest binding energies were visualized with the help of MOE software and the Plip online website. The results are shown in Figure 11.

Table 3 Results of Topological Analysis of Differential Metabolites

No.	Pathway Name	Match Status	*P*	Impact	Match Metabolites
1	Arginine biosynthesis	2/14	0.015	0.117	L-Glutamic acid, Fumaric acid
2	Pyrimidine metabolism	3/39	0.015	0.191	Deoxyuridine, Uracil, Thymidine
3	Primary bile acid biosynthesis	3/46	0.024	0.034	25-Hydroxycholesterol, Glycochenodeoxycholic acid, Chenodeoxycholic acid
4	Riboflavin metabolism	1/4	0.055	0.5	Riboflavin
5	Glutathione metabolism	2/28	0.056	0.044	L-Glutamic acid, gamma-Glutamylcysteine
6	Alanine, aspartate and glutamate metabolism	2/28	0.056	0.2	Fumaric acid, L-Glutamic acid

(*Continued*)

Table 3 (Continued).

No.	Pathway Name	Match Status	*P*	Impact	Match Metabolites
7	Glycine, serine and threonine metabolism	2/34	0.079	0.114	Betaine, Dimethylglycine
8	D-Glutamine and D-glutamate metabolism	1/6	0.081	0.5	L-Glutamic acid
9	Glycerophospholipid metabolism	2/36	0.088	0.017	Acetylcholine
10	Tryptophan metabolism	2/41	0.109	0.094	Indolepyruvate, L-Kynurenine
11	Tyrosine metabolism	2/42	0.114	0.025	Homovanillic acid, Fumaric acid
12	Citrate cycle (TCA cycle)	1/20	0.246	0.03	Fumaric acid
13	Glycolysis / Gluconeogenesis	1/26	0.308	0.001	Alpha-D-Glucose
14	Galactose metabolism	1/27	0.317	0.029	Alpha-D-Glucose
15	Arginine and proline metabolism	1/38	0.417	0.086	L-Glutamic acid
16	Valine, leucine and isoleucine degradation	1/40	0.433	0.023	Methylmalonic acid

Statistical Analyses

All data were analyzed using SPSS (version 25), and the results were expressed as mean ± standard deviation. Comparisons between two groups were performed by *t*-test, and comparisons between multiple groups were performed by one-way ANOVA, with differences considered statistically significant at $P < 0.05$.

Results

Identification and Analysis of the Chemical Compositions in vitro of RR

We conducted positive and negative ion scans on the RR samples following a previously established method, resulting in a total ion flow diagram (TIC), as illustrated in Figure 1. A total of 28 chemical constituents were identified, comprising 11 flavonoids, 7 coumarins, 4 polyphenols, 4 esters, and 2 phenylpropanoids. Three of these chemical constituents were

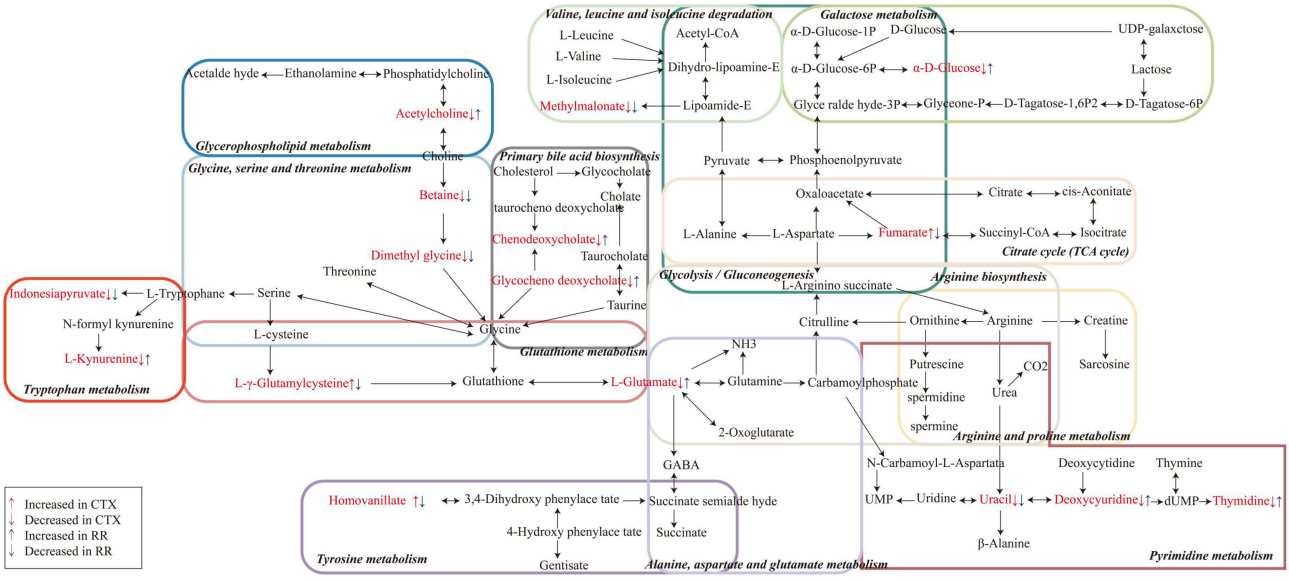

Figure 9 Metabolic pathway network diagram of key differential metabolites. Red-flagged substances are key differential metabolites.

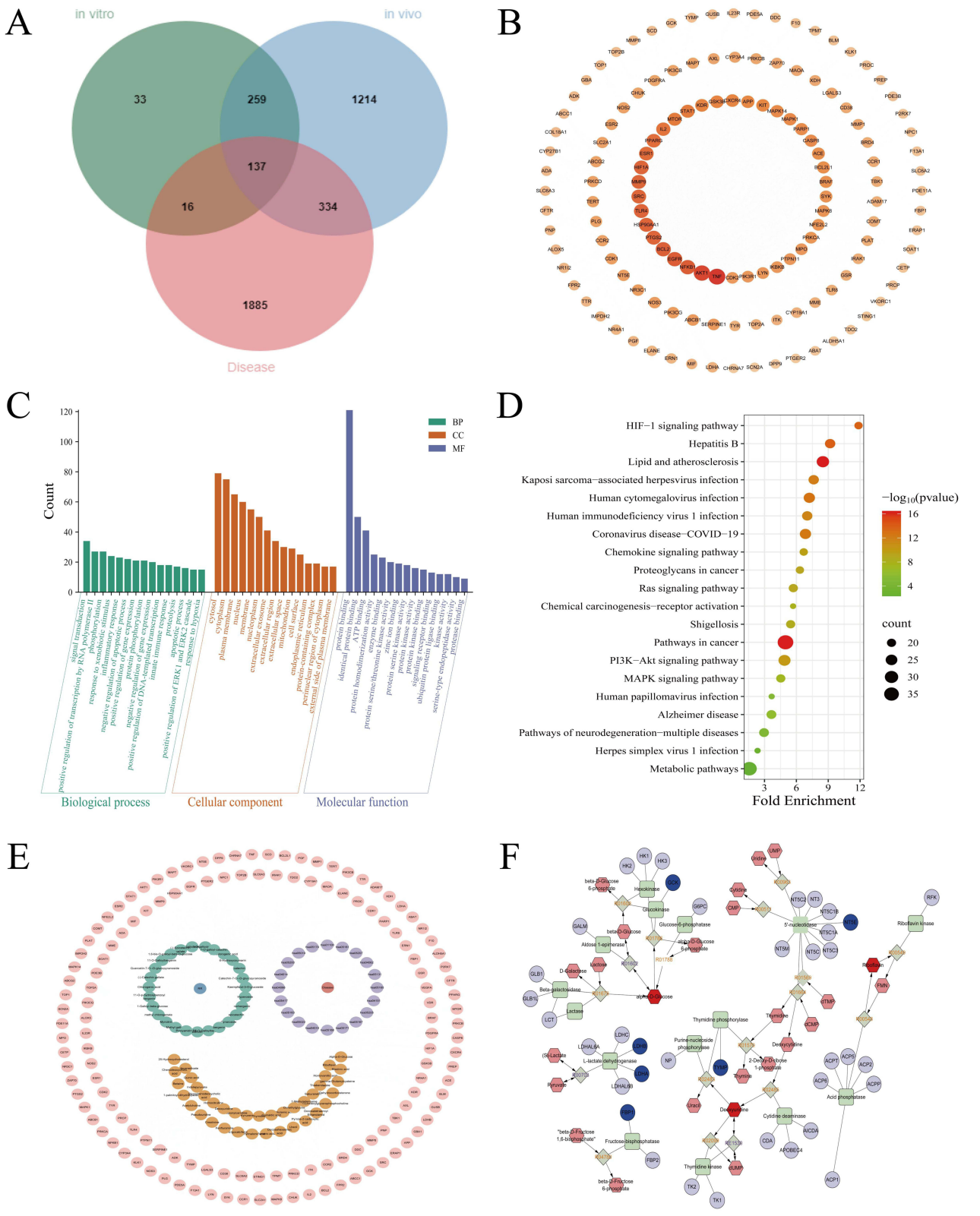

Figure 10 Network pharmacology coanalysis of components in vitro, differential metabolites, and diseases. (**A**): three intersection target genes; (**B**): PPI network diagram, darker color, and larger circle represent higher degree value; (**C**): GO enrichment analysis; (**D**): KEGG analysis; (**E**): "drug-components in vitro-differential metabolites-disease-pathways" network, blue is herb, green is components in vitro, dark pink is disease, purple is pathway. (**E**): "drug-disease-pathways" network, blue is herb, green is components in vitro, dark pink is a disease, purple is the pathway, Orange is a differential metabolite, light pink is intersection target; (**F**): Subnetwork diagram of "Metabolites-Reactions-Enzymes-Genes".

Table 4 The top 15 core target genes

No.	Target	Degree Value	UniProt ID	PDB ID
1	TNF	192	P01375	5UUI
2	AKT1	178	P31749	1UNQ
3	NFKB1	148	P19838	2O61
4	EGFR	148	P00533	8A27
5	BCL2	146	P10415	6GL8
6	HSP90AA1	136	P07900	2YI7
7	PTGS2	136	P35354	5F19
8	TLR4	136	O00206	4G8A
9	MMP9	134	P14780	6ESM
10	SRC	134	P12931	1FMK
11	HIF1A	134	Q16665	4AJY
12	ESR1	130	P03372	1ERR
13	PPARG	126	P37231	1ZGY
14	IL2	118	P60568	1M4A
15	MTOR	108	P42345	5GPG

identified through control comparisons, and the specific results are presented in Table 1. The cleavage pathways are demonstrated using standards as examples, and the results are presented in Supplementary Figures 1–3. In addition, by comparing the peak area with that of the control, the yield of the dry extract was calculated to be 41%, and the content of Bergenin was determined to be 21%.

Therapeutic Role of RR in Immunosuppression

Biochemical Index Determination Findings

We analyzed the collected blood samples and measured three components of whole blood (WBC, RBC, and PLT), immunoglobulins (IgG and IgM), and immune cytokines (IL-2 and IL-6). The results are presented in Figure 3. In each index, the results for the CTX group were significantly lower than those of the control group ($P < 0.01$). Compared to the CTX group, the LMS group exhibited a significant rebound in all measured parameters ($P < 0.01$). Additionally, the various dose administration groups demonstrated varying degrees of rebound ($P < 0.05$, $P < 0.01$); however, the rebound trend was most pronounced in the positive group, which displayed a highly significant rebound ($P < 0.01$). Despite the overall similarity of the results, some subtle differences were observed. For instance, compared to the CTX group, the low-dose administration group did not show significant differences in the three indices of whole blood and immunoglobulins, but it did exhibit substantial differences in immune cytokines ($P<0.05$). Overall, the administration groups mitigated the immunosuppression induced by cyclophosphamide in rats to varying degrees, demonstrating a certain degree of dose dependence, with the high-dose group exhibiting the most significant effect.

Histologic and Pathologic Analysis

As shown in A and B of Figure 4, the organ indices of the thymus and spleen in the model group showed a highly significant reduction ($P < 0.01$) compared to the blank control group. All dose administration groups showed positive

Table 5 Molecular Docking Results of Components in vitro with Core Targets

No.	Active Ingredients	TNF	AKT1	NFKB1	EGFR	BCL2	HSP90AA1	PTGS2	TLR4	MMP9	SRC	HIF1A	ESR1	PPARG	IL2	MTOR
1	6-O-galloyl glucose	−4.5	−5.8	−5.7	−7.9	−5.3	−6.9	−4.3	−5.4	−9.1	−7.1	−5.6	−7	−7	−5.3	−6.7
2	1-Galloyl-beta-glucose	−5.1	−6.2	−6.2	−8.2	−5.5	−8.1	−4.9	−5.1	−10	−7.1	−6.6	−7.9	−7	−5.5	−7.2
3	Gallic acid	−4.1	−4.6	−6.1	−6.5	−4.6	−6.3	−3.9	−4	−7.1	−6.5	−5.5	−5.8	−5.4	−4.4	−5.7
4	Norbergenin	−4.5	−6	−6.9	−7.7	−6.1	−7.5	−5.2	−5.4	−7.1	−7	−6.4	−7.4	−7.1	−5.3	−7.9
5	Catechin-7-O-β-D-glucopyranoside	−5.5	−6.7	−7.4	−8.5	−7.4	−8.8	−5.9	−6.2	−9.9	−7.5	−6.6	−8.4	−8.8	−6.5	−9.6
6	Neochlorogenic acid	−5.1	−6.3	−6.7	−9	−6.4	−8.1	−5.3	−5.1	−10.1	−7	−6.1	−7.6	−7.6	−5.7	−8.1
7	Procyanidin B2	−5.4	−7.2	−7.3	−8.3	−7.9	−8.6	−5.4	−6	−7.9	−6.7	−7.2	−7.3	−3.8	−5.8	−10.3
8	Bergenin	−4.4	−5.9	−6.7	−7.9	−5.6	−7.5	−4.8	−5.1	−6.8	−7	−6.5	−5.7	−7.2	−5.2	−7.9
9	1,6-bis-O-galloyl-beta-D-glucose	−4.6	−6.1	−8.3	−9.6	−6.5	−9.3	−5.2	−5.9	−10.8	−7.5	−7.1	−8.9	−8.4	−6	−8.4
10	Catechin	−5.1	−6	−6.7	−9.4	−7.3	−7.8	−4.8	−5.2	−9	−6.8	−6.2	−8	−7.6	−5.8	−7.9
11	Chlorogenic acid	−5	−6.7	−6.6	−9.1	−6.4	−8.1	−5.2	−5.4	−10.3	−7	−6.7	−7.9	−7.9	−5.9	−8.6
12	6-Hydroxycoumarin	−4.3	−5.2	−5.6	−7.4	−5.7	−6.8	−4.2	−4.5	−8.2	−6.9	−4.9	−6.7	−6.3	−5.5	−7
13	Methyl gallate	−4.1	−4.7	−5.3	−6.7	−4.7	−6.5	−4	−3.9	−7.1	−6.8	−5.6	−5.9	−5.7	−4.4	−5.9
14	Epicatechin	−4.9	−6.1	−6.5	−9.1	−6.7	−8.2	−5	−5	−8.8	−6.8	−6.4	−7.8	−7.9	−6.4	−8.4
15	11-O-Galloylbergenin	−5.4	−7.3	−7.5	−9.2	−6.5	−9.3	−5.6	−6.2	−10.3	−7	−7.2	−7.9	−8.7	−6	−9.8
16	Methyl chlorogenate	−4.9	−6.5	−6.5	−9.1	−6.6	−8.1	−4.9	−5.2	−10.2	−6.7	−6.8	−7.4	−8.2	−6	−8.7
17	4-O-Galloylbergenin	−5	−6.7	−7.6	−8.3	−6.8	−8.8	−5.5	−6.1	−9.7	−8.2	−7	−7.1	−8.1	−5.5	−9.2
18	7-O-galloyl-catechin	−6	−6.8	−7.6	−9.7	−8.1	−9.1	−5.5	−6.3	−11.1	−7.4	−7.5	−9.1	−9.1	−7.2	−9.4
19	(-)-Epicatechin gallate	−5.7	−7.3	−7.7	−8.7	−7.1	−10	−5.2	−5.7	−9.4	−7.9	−7.5	−7.5	−8.9	−6.1	−10
20	(-)-Catechin gallate	−5.2	−7.2	−8.1	−8.9	−7.4	−9.2	−5.5	−5.7	−10.2	−8	−7.2	−10.6	−8.9	−6.7	−9.5

21	Myricitrin	−5	−6.7	−7.1	−7.9	−6.7	−9.1	−5.6	−5.7	−10.1	−7.6	−7.2	−9.5	−8.4	−5.6	−9.4
22	Quercetin-7-O-β-D-glucopyranoside	−5.5	−6.4	−7.3	−10.7	−6.9	−8.8	−5.7	−6.3	−10.9	−8	−7	−7.9	−8.7	−5.7	−9.2
23	Hyperoside	−5	−6.3	−6.7	−7.7	−7.2	−9.2	−5.5	−5.6	−9.2	−7	−7	−7	−8.7	−5.8	−9.3
24	Quercitrin	−5.6	−6	−6.9	−8	−6.6	−9.4	−5.7	−6	−9.7	−7.4	−6.7	−8.8	−9	−5.6	−9.1
25	11-O-p-hydroxybenzoyl bergenin	−5.2	−6.8	−7.1	−7.6	−6.7	−9.1	−5.4	−6.1	−10.2	−7.1	−7.2	−7.3	−8.8	−6.3	−9
26	Kaempferol-3-O-glucoside	−5.4	−6.1	−6.5	−7.7	−6.6	−9	−5.1	−5.3	−8.1	−7.5	−6.5	−9.9	−8	−5.2	−9
27	Cynaroside	−5.5	−6.6	−7.9	−10.7	−7.6	−9	−6.3	−6.3	−11.1	−7.7	−6.7	−8.2	−9	−6	−9.4

https://doi.org/10.2147/DDDT.S479341

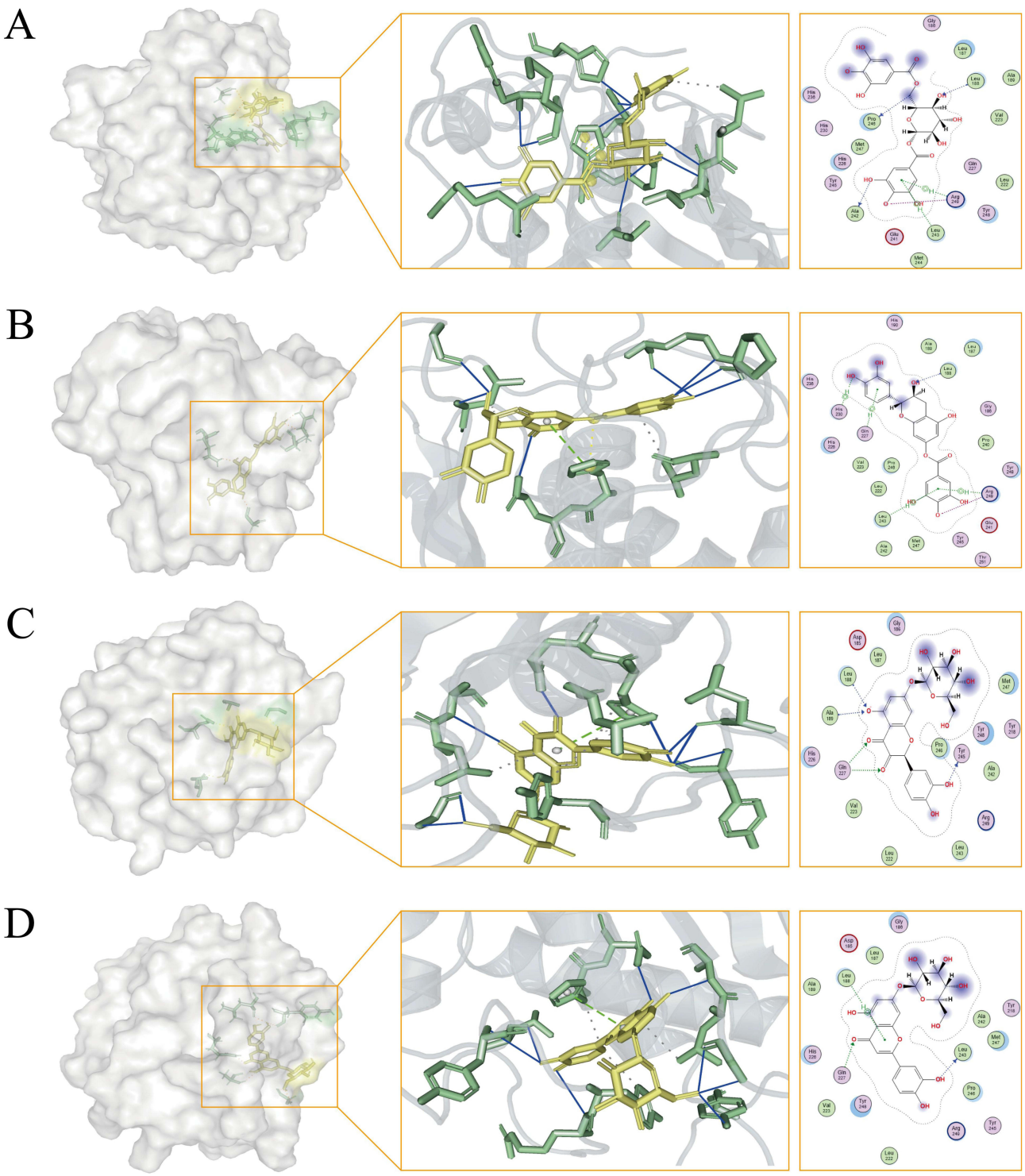

Figure 11 Visual analysis of 3D and 2D results of molecular docking dominant conformations. (**A**): MMP9 and 7-O-galloyl-catechin docking; (**B**): MMP9 and Cynaroside; (**C**): MMP9 and Quercetin-7-O-β-D-glucopyranoside docking; (**D**): MMP9 and 1.6-bis-O-galloyl-beta-D-glucose docking.

immunomodulatory effects compared to the model group, with highly significant effects in the medium-dose and high-dose groups ($P < 0.01$). Still, the degree of recovery was inferior to that of the positive control group.

As shown in Figure 4C, the thymus tissue of control rats was structurally intact, and the boundary between cortex and medulla was visible. The cortex staining was darker, while the medulla staining was lighter. In contrast, in the CTX

group, the thymus medulla was significantly reduced, the boundary between skin and medulla was blurred, and apoptosis was observed. In contrast, thymic tissues in each administration group showed different degrees of recovery, characterized by gradual recovery of the medullary area, improved skin-medullary border definition, and recovery of cortical lymphocytes. Notably, the RR-H and LMS groups showed better recovery.

Histological analysis of the spleen tissue of control rats (Figure 4D) showed well-preserved white and red medullary regions. The white medulla showed dense lymphoid tissue, and the splenic cord and blood sinusoids were well-aligned without apparent abnormalities. In contrast, the white medulla oblongata in the CTX group was significantly reduced in size, and foci of extramedullary hematopoiesis were present in the red medulla. However, compared with the CTX group, both the RR and positive drug groups showed varying degrees of white marrow recovery, reducing extramedullary hematopoietic extent and megakaryocyte counts. Notably, the RR-H and LMS groups showed better recovery.

By thoroughly analyzing the hematological indices, organ indices, and histological results, we can conclude that an immunosuppressive model has been successfully established and that all dosage administration groups exhibited varying degrees of immunomodulatory effects.

Multivariate Statistical Analysis

As shown in A and B in Supplementary Figure 4, the QC samples(n=8) were highly clustered, indicating good instrumental stability and reliable data suitable for subsequent metabolomics data analysis. As can be seen in Figure 5A and B, the groups can be spatially grouped with prominent grouping trends in both positive and negative ion modes. At the same time, we performed the OPLS-DA discriminant analysis with supervised modeling (Figure 5C and D). In the positive ion mode, three principal components were extracted, $Q^2 = 0.692$, $R^2X = 0.264$, and $R^2Y = 0.995$; in the negative ion mode, four principal components were extracted, $Q^2 = 0.832$, $R^2X = 0.344$, and $R^2Y = 0.998$. The above results were verified with 200 permutation tests, and the intercepts were all negative, proving that the model is stable and reliable.

A two-by-two comparison of the three groups was performed to determine the trend of the differential metabolites in vivo, and the results were shown in a volcano diagram (Figure 6). Meanwhile, based on the previous criteria, we identified 37 differential metabolites (Table 2), of which 19 were in the positive ion mode and 18 in the negative ion mode. The results showed that 31 substances were down-regulated, 6 were up-regulated in the CTX group(n=6) compared with the control group(n=6), 22 were up-regulated, and 15 were down-regulated in the RR-H group(n=6) compared with the CTX group(n=6). The changes in the trend are shown in Supplementary Figure 5. Notably, 28 substances showed opposite trends among these compounds, including L-glutamic acid, L-kynurenine, α-D-glucose, riboflavin, and fumaric acid. It is reasonable to hypothesize that these specific compounds play a role in modulating the body's immune response.

We further validated the analysis of the mined differential metabolites using ROC curves to assess the diagnostic accuracy of the identified biomarkers by calculating the area under the ROC curve (AUC). An AUC value between 0.7 and 0.9 indicates a certain level of diagnostic accuracy, whereas an AUC of greater than 0.9 indicates a very high degree of predictive power. In our results (Figure 7), ergocalciferol, fumaric acid, hexadecanedioic acid, thiabendazole, indolepyruvic acid, and fenfluramine showed firm ROC profiles with very high AUC values (all higher than 0.8), and the rest of the substances also showed good performance, with AUC values higher than 0.7.

Metabolic Pathways Analysis of Potential Biomarkers

As shown in Figure 8, a total of 16 pathways were involved in metabolic pathway analysis, including arginine biosynthesis, pyrimidine metabolism, primary bile acid biosynthesis, riboflavin metabolism, glutathione metabolism, alanine, aspartate and glutamate metabolism, D-glutamine and D-glutamate metabolism, glycerophospholipid metabolism, tryptophan metabolism, and tyrosine metabolism. Meanwhile, the results of topological analysis (Table 3) showed that some metabolites were involved in only one or two pathways, such as riboflavin and α-D-glucose. While some metabolites, such as L-glutamate and fumaric acid, play a regulatory role in multiple metabolic pathways. Integrating the above results thus forms a metabolic network that explains the process of metabolic changes in organisms (Figure 9).

Integrated Analysis of Network Pharmacology, Molecular Docking, and Metabolomics

Based on the Q-TOF results, we identified 28 components in vitro and conducted subsequent target analyses for 27 substances that are detectable in the PubChem database (Supplementary Table 1). Targets from various databases were combined and de-emphasized, yielding 446 targets. Similarly, targets for different metabolites were collected, resulting in 1944 targets after de-emphasis. The disease targets retrieved from the database were organized, leading to the identification of 2372 targets. By matching the targets mentioned above with the identified disease targets, we found 137 crossover genes.

Using Cytoscape software, we constructed a network diagram illustrating the relationships among 27 components, 37 differential metabolites, and the top 20 pathways, referred to as the "drug-components-differential metabolites-disease-pathways" network. Simultaneously, we analyzed the differential metabolites associated with the three cross-targets (TOP 15) using the MetScape plug-in, which yielded results for the "compound-reaction-enzyme-gene" interactions. Subsequently, we integrated these findings with the differential metabolite pathways analyzed on the MetaboAnalyst platform to identify the crossover pathways. We conducted an in-depth analysis of four pathways: galactose metabolism, glycolysis/gluconeogenesis, pyrimidine metabolism, and riboflavin metabolism. The results of the associated subnetworks are presented in Figure 10F.

The binding energy's magnitude indicates the complex molecule's binding capacity. Generally, binding energies less than −5 kcal/mol are considered acceptable, while those below −7 kcal/mol are regarded as exhibiting binding solid activity.[50] In the present study, the molecular docking method was employed to investigate the regulatory effects of 7-O-galloyl-catechin, Cynaroside, Quercetin-7-O-beta-D-glucopyranoside, and 1.6-bis-O-galloyl-beta-D-glucose on MMP9 (Figure 11). All of these compounds demonstrated binding energies lower than −7 kcal/mol. Therefore, it can be hypothesized that RR may influence MMP9 through these four substances (7-O-galloyl-catechin, Cynaroside, Quercetin-7-O-beta-D-glucopyranoside, and 1.6-bis-O-galloyl-beta-D-glucose), thereby exerting immunomodulatory effects by impacting four critical pathways: galactose metabolism, glycolysis/glycogenesis, pyrimidine metabolism, and riboflavin metabolism.

Discussion

We conducted a study investigating the role of RR in regulating the organism's immunosuppressive state. The study was divided into four stages. First, we characterized the chemical composition of RR using the UPLC-Q-TOF MS/MS technique. Next, we established an immunosuppressed rat model using cyclophosphamide, and we verified the efficacy of RR through physiological and biochemical indices and pathological tissue results. Subsequently, we employed non-targeted metabolomics to identify potential biomarkers in rat serum. Significant differential metabolites were screened by combining multivariate statistical analyses to explore critical metabolic pathways and elucidate the mechanism of action in vivo by mapping the immunomodulatory network. Finally, we applied network pharmacology and molecular docking techniques to integrate the metabolomics data with the components in vitro, constructing a network of "drug-components -differential metabolites-disease-pathways" to reveal how the internal and external components work together to influence the organism's immunity.

The human immune system can be categorized into specific and non-specific immunity, which involves the synergistic action of various cells, organs, and systems. The absence of any one component may lead to dysregulation of immune function. Cyclophosphamide, a nitrogen mustard alkylating agent used in cancer treatment, can cause bone marrow suppression with prolonged use, resulting in a decrease in leukocytes and hemoglobin levels in the peripheral blood, thereby inducing a state of immunosuppression. Research has demonstrated that levamisole hydrochloride exerts a positive modulatory effect on immunosuppressed mice, making it a potential immunomodulator.[51,52] In the specific immune response, T lymphocytes stimulate the secretion of cytokines (eg, IL-2 and IL-6) and play a crucial role in cellular immunity, while B lymphocytes differentiate into plasma cells and enhance humoral immunity through the production of immunoglobulins (IgG and IgM). IL-2, a pro-inflammatory factor produced by the Th1 subpopulation, and IL-6, an anti-inflammatory factor produced by the Th2 subpopulation, interact to regulate the balance between Th1 and Th2 cells, thereby maintaining an optimal state of cellular immunity.[53]

In the present study, we observed a significant decrease in hematological parameters in the CTX group compared to the control group. Combined with histological analysis, these results collectively indicate that we successfully established an immunosuppressive model. Following a period of RR treatment, IL-2, IL-6, IgG, and IgM levels increased significantly, particularly in the high-dose group. The organ indices and pathological results from each group further confirmed that RR could enhance the immune function of the organism, aligning with our anticipated outcomes.

We found that the involvement of RR in immunomodulation is a complex process, so we performed an untargeted metabolomics analysis of Serum from a high-dose group of rats to elucidate its biological significance by mining potential biomarkers. A total of 37 potential biomarkers were identified in this study, and subsequent pathway enrichment and topological analysis revealed that they were involved in acting on 16 metabolic pathways, including arginine biosynthesis, pyrimidine metabolism, primary bile acid biosynthesis, riboflavin metabolism, and glutathione metabolism. Based on this, we constructed an immunoregulatory network map containing multiple metabolites and pathways to elucidate the mechanism of action of RR.

However, metabolomics technology has certain limitations regarding the metabolites and metabolic pathways involved, and it cannot fully elucidate their associated mechanisms. Therefore, we integrated network pharmacology and molecular docking techniques to correlate the identified chemical components in vitro and the differential metabolites in vivo with the target diseases. By using intersecting targets and co-acting pathways as entry points, we constructed a more intricate network to investigate how components in vitro influence diseases through substances in vivo and pathways. The results of molecular docking indicated that the compounds in vitro primarily acted through flavonoids, coumarins, and polyphenols, which largely aligned with the previous findings from Q-TOF compositional analysis. In addition, the phenomenon whereby the same target effectively docks with various components, and the same component effectively docks with multiple targets, has been observed. This observation confirms the theory that the mechanism of action of traditional Chinese medicine is complex, exerting its efficacy through various targets and pathways.

Studies have demonstrated that flavonoids possess a range of pharmacological activities, including anti-inflammatory, antioxidant, antitumor, and immune function modulation.[13–16] These compounds can enhance the immune microenvironment of the body and improve the immune response by increasing the weight and volume of immune organs,[15] promoting the production and secretion of immunoglobulins such as IgG and IgA, and simultaneously upregulating the expression of interleukins IL-2 and IL-6.[16] Polyphenols can influence cellular immunity by enhancing the T-lymphocyte conversion rate[54] while modulating humoral immunity by promoting the expression of IgG and IgM immunoglobulins.[55] Together, these two mechanisms play a crucial role in the body's immunoregulation. Coumarins modulate the secretion of inflammatory factors (eg IL-2 and IL-6)by decreasing the levels of inflammatory mediators (eg nitric oxide) and arachidonic acid,[56,57] which ameliorates inflammation and thus affects the immune function of the body. In addition, they showed significant effects in regulating T-cell proliferation and splenic lymphocyte proliferation.[58]

Glycolysis/Gluconeogenesis

As the most prevalent monosaccharide, glucose is the primary source of energy production and macromolecular biosynthesis in organisms.[59] Under aerobic conditions, its metabolism yields pyruvate, which can be converted into acetyl Coenzyme A and carbon dioxide through the pyruvate dehydrogenase complex,[59,60] a process known as aerobic glycolysis. Acetyl coenzyme A can combine with oxaloacetic acid to generate citric acid and participate in the Krebs cycle.[61] In hypoxic conditions, pyruvate is catalyzed by lactate dehydrogenase to form lactic acid,[59] thereby contributing to energy metabolism. Alanine, primarily produced by skeletal muscle and red blood cells, is a significant gluconeogenesis precursor, promoting muscle growth, enhancing immunity, and facilitating wound healing.[62,63] A reversible reciprocal conversion between alanine and pyruvate exists; under the influence of alanine aminotransferase, pyruvate can be transformed into alanine or vice versa through deamination.[64,65] The observed significant change in glucose levels before and after administration may be closely associated with inhibition of the glycolysis pathway and stimulation of gluconeogenesis pathway catalysis.

Furthermore, down-regulation of fumaric acid content promotes the TCA cycle to some extent by rapidly replenishing intermediate metabolites involved in metabolism such as tryptophan, L-proline, and glutamic acid-all serving as substrates for nucleotide biosynthesis-thus influencing immune regulation.[66] Free amino acids play a crucial role as

precursors for gluconeogenesis;[67] our findings suggest that elevated glutamate levels provide ample raw materials for this process. Overall, glycose metabolism intricately interacts with the TCA cycle and remains inseparable; ATP generated during this process is efficiently recycled within the body to maintain cellular physiological functions.

Pyrimidine Metabolism

Pyrimidine metabolism regulates nucleotide homeostasis through de novo synthesis, catabolism, salvage, and recovery.[68] In the body, uracil is derived partly from urea interconversion and partly from β-alanine metabolism. As an isomer of alanine, β-alanine plays a role in steroid hormone regulation by activating glycine and gamma-aminobutyric acid (GABA) receptors.[69] Hypoxanthine can be converted into uric acid through its purine metabolic pathway,[70] serving as the end product of purine metabolism.[71] Simultaneously, under the action of uricase, uric acid can be converted into glutamic acid.[72] The nitrogenous derivative of histidine, known as histamine, can undergo deamination through the action of histidine ammonia and actively participate in the inflammatory response within the body.[70] Following RR administration, rat immune levels gradually recovered, suggesting a potential reduction in substances contributing to inflammation within the body. Lower histidine levels also lead to decreased uric acid levels, subsequently regulating glutamate levels in the body's system.

In addition to this process, arginine metabolism produces urea, which competes with ornithine synthesis.[72,73] Ornithine can be metabolized into putrescine and further produce spermidine.[74,75] Spermidine interacts with nucleic acids and stabilizes their structure.[70] Our study observed significant down-regulation of uracil after administration, and reduced conversion-produced urea level may result from competitive inhibition between arginine's two metabolic pathways. This may lead to increased ornithine levels promoting spermidine biosynthesis. LanZ et al's study[70] demonstrated that diminished pyrimidine levels affect the nucleic acid structure, potentially leading to elevated spermidine levels consistent with our findings.

Riboflavin Metabolism

Vitamin B2 plays a critical role in energy metabolism and the metabolism of fats, ketone bodies, carbohydrates, and proteins.[76,77] Riboflavin, as a member of the vitamin B family, can not only act as a precursor to participate in the formation of FMN and FAD but also involve a variety of metabolic pathways. Riboflavin supplementation has biological implications for enhancing the synthesis of other B vitamins, in particular B6 (which requires FMN to function) and B3 (niacin) (which requires FAD to form from tryptophan).[77] Riboflavin affects tryptophan metabolism and increases riboflavin levels, increasing sarcosine levels.[77] Then, threonine production into betaine regulates the body's immunity.[78,79] In our study, riboflavin content was significantly increased in the administration group, suggesting that riboflavin and its metabolism are essential to immune regulation. However, the specific mechanism of action still needs to be further studied.

Although we have utilized integrated research to investigate the bases in vitro and in vivo material and metabolic pathways through which RR may exert its effects on disease, additional follow-up experiments are necessary to validate the analysis further.

Conclusion

Overall, we utilized bioinformatics technology for the first time to analyze the relationship between components in vitro and in vivo and diseases, and we verified the role of RR in immunomodulation through animal experiments. Additionally, we successfully identified 28 chemical components, 37 potential biomarkers, and 15 core targets, including MMP9, EGFR, and MTOR. The results suggest that RR may interact with the target protein MMP9 through flavonoid, coumarin, and polyphenol components, thereby influencing four key pathways: galactose metabolism, glycolysis/gluconeogenesis, pyrimidine metabolism, and riboflavin metabolism, which contribute to its immunomodulatory functions. This finding opens new avenues for the in-depth study of the molecular mechanisms of traditional Chinese medicine (TCM).

Abbreviations

TCM, traditional Chinese medicine; UPLC, ultra-high performance liquid chromatography; Q-TOF, quadrupole time of flight; MS, mass spectrometry; CTX, cyclophosphamide; KEGG, Kyoto Encyclopedia of Genes and Genomes; RR,

Rhizoma Rodgersiae; TIC, Total Ion Chromatogram; SD, Sprague-Dawley; RR-L, RR-Low; RR-M, RR-medium; RR-H, RR-high; LMS, levamisole; CMC-Na, Carboxy Methyl Cellulose Sodium; HE, hematoxylin and eosin; WBC, white blood cell; RBC, red blood cell; PLT, blood platelet; IgG, Immunoglobulin G; IgM, Immunoglobulin M; IL-2, Interleukin-2; IL-6, Interleukin-6; ELISA, enzyme-linked immunosorbent assay; ESI, Essential Science Indicators; HMDB, Human Metabolome Database; PCA, principal component analysis; OPLS-DA, orthogonal partial least squares discriminant analysis; QC, Quality Control; VIP, Variable importance in the projection; FC, Fold Change; ROC, Receiver Operating Characteristic; TTD, Therapeutic Target Database; OMIM, Online Mendelian Inheritance in Man; PPI, Protein-protein interaction; GO, Gene Ontology; FDR, false discovery rate; MOE, Molecular Operating Environment; Plip, Protein-Ligand Interaction Profiler; ANOVA, Analysis of Variance; AUC, Area under the curve; TCA, tricarboxylic acid cycle; ATP, adenosine triphosphate; GABA, gamma-aminobutyric acid; FMN, flavin mononucleotide; FAD, Flavin adenine dinucleotide.

Acknowledgments

I would like to thank Dali University for providing experimental facilities. I would also like to thank my teachers and other students in the group for their help and support.

Author Contributions

All authors made a significant contribution to the work reported, whether that is in the conception, study design, execution, acquisition of data, analysis, and interpretation, or all these areas; took part in drafting, revising, or critically reviewing the article; gave final approval of the version to be published; have agreed on the journal to which the article has been submitted; and agree to be accountable for all aspects of the work.

Funding

This research work was financially supported by the National Natural Science Foundation of China (Accession no. 81560695), the Special Basic Cooperative Research Programs of Yunnan Provincial Undergraduate Universities'Association (202101BA070001-217 and 202101AO070268), research program of Yunnan Provincial Key Laboratory of Entomological Biopharmaceutical R&D (AS2022001) and support program of Xingdian Talent.

Disclosure

The authors declare no potential conflicts of interest for this work.

References

1. Wang Y, Jin Y, Liu ZQ. Optimization of the extraction process of bergenin from *Rodgersia pinnata*. *J Dali Univ*. 2012;11(9):8–10.
2. Liu R, Zhao YC, Ke FX, et al. Determination of bergeninum in *Rodgersia sambucifolia* Hemsl from different source by HPLC. *Res Prac Chinese Med*. 2014;28(2):13–15. doi:10.13728/j.1673-6427.2014.02.006
3. Yang YX, Zhuang FF, Yan FL. Synthesis and anti-tumour activity evaluation of bergenin derivatives. *J Xinxiang Medical*. 2019;36(9):819–823.
4. Jahromi MAF, Chansouria JPN, Ray A. Hypolipidaemic activity in rats of bergenin, the major constituent of flueggea microcarpa. *Phytother Res*. 1992;6(4):180–183. doi:10.1002/ptr.2650060403
5. Piacente S, Pizza C, De Tommasi N, Mahmood N. Constituents of Ardisia japonica and their in vitro anti-HIV activity. *J Nat Prod*. 1996;59 (6):565–569. PMID: 86362. doi:10.1021/np960074h
6. Nalakshmit S, Amanmg S, Sulochanan. A note on the anti-inflammatory activity of bergenin. *RArivudainambi Curr Sci*. 1984;53(17):917–921.
7. Pu HL, Huang X, Zhao JH, Hong A. Bergenin is the antiarrhythmic principle of *Fluggea virosa*. *Planta Med*. 2002;68(4):372–374. PMID: 11988869. doi:10.1055/s-2002-26758
8. Takahashi H, Kosaka M, Watanabe Y, et al. Synthesis and neuroprotective activity of bergenin derivatives with antioxidant activity. *Bioorg Med Chem*. 2003;11(8):1781–1788. PMID: 12659764. doi:10.1016/s0968-0896(02)00666-1
9. Lim H-K, Kim H-S, Serck Choi H, et al. Hepatoprotective effects of bergenin, a major constituent of Mallotus japonicus, on carbon tetrachloride-intoxicated rats. *J Ethnopharmacol*. 2000;72(3):0–474. doi:10.1016/s0378-8741(00)00260-9
10. Goel RK, Maiti RN, Manickam M, Ray AB. Antiulcer activity of naturally occurring pyrano-coumarin and isocoumarins and their effect on prostanoid synthesis using human colonic mucosa. *Indian J Exp Biol*. 1997;35(10):1080–1083. PMID: 9475044.
11. Wang G, Ma BJ. An overview of the research on bengenin. *J Anhui Univ Chinese Med*. 2002;(06):59–62. doi:10.3969/j.issn.1000-2219.2002.06.027
12. Wu CY, Shu XH, Song CL, et al. The immunomodulatory activity of flavonoids from *Rodgersiae rhizoma* in rats. *J Shenyang Pharmaceut Univ*. 2020;37(11):1037–1042. doi:10.14066/j.cnki.cn21-1349/r.2020.11.011

13. Tao L, Xin L, Xianghua S, et al. The immunomodulatory effects of *Rodgersia sambucifolia* Hemsl. Flavone *Phellodendron chinensis* Schneid. flavone and *Angelica sinensis* polysaccharose complex on immunosuppressive rats. *J Trad Chinese Vet Med*. 2021;40(04):18–22. doi:10.13823/j.cnki.jtcvm.2021.04.004
14. JW W, YP F, ZH S, et al. Effects of total flavonoids of *Astragalus* on immune function and cytokines in rats with Pneumocystis carinii pneumonia. *Chin J Ctrl Endem Dis*. 2023;38(04):335–337.
15. Zhao L. The effect of isoflavones of minshan red clover on immunefunction and exercise capacity in exercise rats. *Bull SportSci Tech*. 2024;32(01):265–267. doi:10.19379/j.cnki.issn.1005-0256.2024.01.067
16. Chen WY, LI L, Guo EC, et al. Effect of *Phyllanthus emblica* L. total flavonoids on immunomodulatory function in H22 tumor-bearing mice. *Chin J Hospital Pharm*. 2024;44(16):1851–1859. doi:10.13286/j.1001-5213.2024.16.02
17. Shi YB, Hu ZY, Dong PC, et al. Progress of Modern research on *Herbal Rodgersia aesculifolia Batal*. *Lishizhen Med Materia Medica Res*. 2004;2004(09):621–622.
18. Zhang XY, Li DW, Wang YC, et al. Distribution and medical value of *Rodgeris aesculifolia* and its exploitation. *Subtrop Plant Sci*. 2005;34(02):60–62.
19. Hu FL, Liu H. Current status of research on the Chinese medicinal herb *Rodgersia aesculifolia*. *Shaanxi J Agri Sci*. 2008;5(03):144–145.
20. Zhang DJ. Research Status of *Rodgersia aesculifolia* and Resources Utilization. *Res Prac Chinese Med*. 2012;26(02):16–18. doi:10.13728/j.1673-6427.2012.02.011
21. Zhang M, Feng B, Zhou BK, et al. Overview of pharmaceutical research on *Rodgersia aesculifolia* bata. *J Anhui Agric Sci*. 2015;43(01):33–35. doi:10.13989/j.cnki.0517-6611.2015.01.021
22. Xie JL, Sun J, Lu Y, et al. Research progress on *Rodgersia Sambucifolia*. *Chin J Ethnomedicine Ethnopharm*. 2022;31(12):72–81. doi:10.1186/s13002-022-00572-2
23. LW H, SJ C, Dong R, et al. Progress of network pharmacology applications in studying the complex mechanisms of action of traditional Chinese medicine. *Shandong Sci*. 2021;34(06):22–31. doi:10.3976/j.issn.1002-4026.2021.06.004
24. Li G, JC Z. Applicatoin progress on click chemistry in targets identification of bioactive components from Chinese materia medica. *Chin Trad Herbal Drugs*. 2019;50(04):984–991.
25. Liu ZH, Sun XB. Network pharmacology: new opportunity for the modernization of traditional Chinese medicine. *Acta Pharma Sin*. 2012;47(06):696–703. doi:10.16438/j.0513-4870.2012.06.001
26. Zhu RL, Shen Y, Ma FH, et al. Application of molecular docking in screening of anti-inflammatory constituents of traditional Chinese medicine and their mechanisms. *Chin J Pharmacol Toxicol*. 2018;32(6):10.
27. Tian Y, Wang Z, Liu X, et al. Prediction of chemotherapeutic efficacy in non-small cell lung cancer by serum metabolomic profiling. *Clin Cancer Res*. 2018;24(9):2100–2109. doi:10.1158/1078-0432.CCR-17-2855
28. Lima AR, Pinto J, Amaro F, et al. Advances and perspectives in prostate cancer biomarker discovery in the last 5 years through tissue and urine metabolomics. *Metabolites*. 2021;11(3): 181. doi:10.3390/metabo11030181
29. FANG Q, WANG Y. Chemical differentiation of three Saxifragaceae medicinal plants for traditional Chinese medicine "Yan-tuo" using ultra high performance liquid chromatography-electrospray ionization-quadrupole-time-of-flight mass spectrometry. *Latin Am J Pharm*. 2020;39(9):1715.
30. TL C, XL M, YF Z, et al. Rapid analysis components of Tuihuang mixture based on UHPLC-Q-exactive orbitrap MS. *J Guangdong Pharmaceut Univ*. 2024;40(03):54–62. doi:10.16809/j.cnki.2096-3653.2024031402
31. Ren H, Hu J, X CUI, X LIU, Z CHEN. Analysis on chemical constituents in rhizomes of *Bergenia scopulosa* byUHPLC-Q Exactive focus MS/MS. *Chin J Exp Trad Med Formul*. 2021;27(09):118–128. doi:10.13422/j.cnki.syfjx.20210146
32. Xie Y, Li B. Analysis of chemical constituents in kanglao capsule by UHPLC-Q-TOF-MS/MS. *Chinese Trad Patent Med*. 29:1–9.
33. Li RS, Li SY, Liu W, et al. Analysis of chemical constituents of *Agrimonia pilosa* based on UHPLC-Q-exactive orbitrap HRMS technology. *J Shenyang Pharmaceut Univ* 2024;6:1–14. doi:10.14066/j.cnki.cn21-1349/r.2023.1310
34. YL Z, MQ C, WQ P, et al. Comparison of the chemical compositions and blood constituents of the aqueous and alcoholic extracts of *Hypericum perforatum* L. based on UPLC-Q-TOF-MS/MS. *J Chinese Med Mater*. 2024;47(02):375–382. doi:10.13863/j.issn1001-4454.2024.02.019
35. Cai DJ. Chemical constituents and COX-2 inhibitory activity of *Bergenia purpurascens*. *Jiangxi Univ Chinese Med*. 2023. doi:10.27180/d.cnki.gjxzc.2023.000497
36. FR D, XY J, XH W, et al. Chemical composition, antioxidant, enzyme inhibitory and anti-inflammatory activities of *Hedychium flavum* flower. *Nat Prod Res Dev*. 2024;36(01):13–25. doi:10.16333/j.1001-6880.2024.1.002
37. CL S, Wu H, TL L, et al. Analysis of the chemical constituents of aboveground parts of *Tetrastigma hemsleyanum* by UPLC-Q-TOF-MS method. *Chinese Trad Patent Med*. 2018;40(06):1424–1429.
38. Li RQ, LIu JH, Chen C, et al. An analysis of chemical components of tongluo yiqing prescription based on ultra-performance liquid chromatography-orbitrap-mass spectrometry/massSpectrometry. *J Anhui Univ Chinese Med*. 2024;43(04):100–107.
39. Fang QQ, Wang Y. Identification of multi-source ethnodrug rodgersiae rhizoma by DNABarcoding technology. *Chin J Exp Trad Med Formul*. 2020;26(17):142–150. doi:10.13422/j.cnki.syfjx.20201811
40. Demurtas A, Pescina S, Nicoli S, Santi P, Ribeiro de Araujo D, Padula C. Validation of a HPLC-UV method for quantifying budesonide in skin layers. *J Chromatogr B Analyt Technol Biomed Life Sci*. 2021;1164:122512. doi:10.1016/j.jchromb.2020.122512
41. Zelena E, Dunn WB, Broadhurst D, et al. Development of a robust and repeatable UPLC-MS method for the long-term metabolomic study of human serum. *Analyt Chem*. 2009;81:1357–1364. doi:10.1021/ac8019366
42. J WE, Masson P, Michopoulos F, et al. Global metabolic profiling of animal and human tissues via UPLC-MS. *Nat Protoc*. 2013;8(1):17–32. doi:10.1038/nprot.2012.135
43. Smith CA, Want EJ, O'Maille G, Abagyan R, Siuzdak G. XCMS: processing mass spectrometry data for metabolite profiling using nonlinear peak alignment, matching, and identification. *Anal Chem*. 2006;78(3):779–787.doi:10.1021/ac051437y.
44. Navarro-Reig M, Jaumot J, García-Reiriz A, et al. Evaluation of changes induced in rice metabolome by Cd and Cu exposure using LC-MS with XCMS and MCR-ALS data analysis strategies. *Anal Bioanal Chem*. 2015;407(29):8835–8847. doi:10.1007/s00216-015-9042-2
45. Wishart DS, Tzur D, Knox C, et al. HMDB: the human metabolome database. *Nucleic Acids Res*. 2007;35:D521–D526. doi:10.1093/nar/gkl923
46. Horai H, Arita M, Kanaya S, et al. MassBank: a public repository for sharing mass spectral data for life sciences. *J Mass Spectrom*. 2010;45(7):703–714. doi:10.1002/jms.1777

47. Sud M, Fahy E, Cotter D, et al. LMSD: LIPID MAPS structure database. *Nucleic Acids Res*. 2007;35:D527–D532. doi:10.1093/nar/gkl838
48. Abdelrazig S, Safo L, Rance GA, et al. Metabolic characterisation of magnetospirillum gryphiswaldense MSR-1 using LC-MS-based metabolite profiling. *RSC Adv*. 2020;10(54):32548–32560. doi:10.1039/d0ra05326k
49. Ogata H, Goto S, Sato K, Fujibuchi W, Bono H, Kanehisa MKEGG. Kyoto encyclopedia of genes and genomes. *Nucleic Acids Res*. 1999;27 (1):29–34. doi:10.1093/nar/27.1.29
50. Hsin KY, Ghosh S, Kitano H. Combining machine learning systems and multiple docking simulation packages to improve docking prediction reliability for network pharmacology. *PLoS One*. 2013;8(12):e83922. doi:10.1371/journal.pone.0083922
51. Lin YF, Zhang Q, Gao FF. Effects of levamisole hydrochloride on immune function of immunocompromised mice. *Food Drug*. 2018;20(6):5. doi:10.3969/j.issn.1672-979X.2018.06.017
52. Ye XD, Xu TT, Lu YY, Wang J. Effect of levamisole hydrochloride on the immune function in immunosuppressed mice. *The Chinese J Clin Pharmacol*. 2019;35(6):4. doi:10.13699/j.cnki.1001-6821.2019.06.013
53. Deng XY, Huang JH, Zhao CM, Ma WA, Ge Y, Chen ZB. Effect of astaxanthin on immune function in immunosuppressed mice. *China Animal Husb Vet Med*. 2023;50(09):3519–3529. doi:10.16431/j.cnki.1671-7236.2023.09.008
54. Gao WH. Effect of tea polyphenols on lipometabolism andImmunity function of broiler chickens. *Coll Animal Sci Huazhong Agri Univ*. 2003;2003.
55. Guo CT. Research on the mechanism of metabolic transport and immunomodulation of different dried thinned peach polyphenols. *Shenyang Agri Univ*. 2022. doi:10.27327/d.cnki.gshnu.2022.000179
56. LL K, JF H, Chen NH. Nitric oxide and endothelin: their roles and targeting drugs in vascular diseases. *Chinese Pharmacoll Bull*. 2012;28 (02):165–168.
57. YH W, LIu L, BN Z, et al. Research progress on traditional uses, coumarins, pharmacological activities and toxicology of *Angelica* L. *J Pharm Res*. 2023;42(06):403–408+421. doi:10.13506/j.cnki.jpr.2023.06.010
58. LI HP. Synthesis and antifungal activity of 3-(FluoroSubstitued Phenyl)-3,4-Dihydroisocounmarins. *Northwest Agri Forest Univ*. 2018. doi:10.27409/d.cnki.gxbnu.2018.000288
59. Cai Z, Zhao JS, Li JJ, et al. A combined proteomics and metabolomics profiling of gastric cardia cancer reveals characteristic dysregulations in glucose metabolism. *Mol Cell Proteomics*. 2010;9(12):2617–2628. doi:10.1074/mcp.M110.000661
60. Hyeon JS, Jung Y, Lee G, Ha H, Hwang GS. Urinary metabolomic profiling in streptozotocin-induced diabetic mice after treatment with losartan. *Int J Mol Sci*. 2020;21(23):8969. doi:10.3390/ijms21238969
61. Chashmniam S, Mirhafez SR, Dehabeh M, et al. A pilot study of the effect of phospholipid curcumin on serum metabolomic profile in patients with non-alcoholic fatty liver disease: a randomized, double-blind, placebo-controlled trial. *Eur J Clin Nutr*. 2019;73(9):1224–1235. doi:10.1038/s41430-018-0386-5
62. Chen C, Gao J, Wang TS, et al. NMR-based metabolomic techniques identify the toxicity of emodin in HepG2 cells. *Sci Rep*. 2018;8(1):9379. doi:10.1038/s41598-018-27359-4
63. Zhang H, Zhao L. Influence of sublethal doses of acetamiprid and halosulfuron-methyl on metabolites of zebra fish (Brachydanio rerio). *Aquat Toxicol*. 2017;191:85–94. doi:10.1016/j.aquatox.2017.08.002
64. Guo F, Han M, Lin S, et al. Enteromorpha prolifera polysaccharide prevents high- fat diet-induced obesity in hamsters: a NMR-based metabolomic evaluation. *J Food Sci*. 2021;86(8):3672–3685. doi:10.1111/1750-3841.15818
65. Li G, Zhang X, Qian H, Liu M, Zhao G, Xu A. Gas chromatography-mass spectrometry based midgut metabolomics reveals the metabolic perturbations under NaF stress in bombyx mori. *Insects*. 2019;11(1):17. doi:10.3390/insects11010017
66. Huang FQ, Li J, Jiang L, et al. Serum-plasma matched metabolomics for comprehensive characterization of benign thyroid nodule and papillary thyroid carcinoma. *Int J Cancer*. 2019;144(4):868–876. doi:10.1002/ijc.31925
67. Shin JH, Yang JY, Jeon BY, et al. (1)H NMR-based metabolomic profiling in mice infected with mycobacterium tuberculosis. *J Proteome Res*. 2011;10(5):2238–2247. doi:10.1021/pr101054m
68. Herman S, Åkerfeldt T, Spjuth O, Burman J, Kultima K. Biochemical differences in cerebrospinal fluid between secondary progressive and relapsing‐remitting multiple sclerosis. *Cells*. 2019;8(2):84. doi:10.3390/cells8020084
69. Lu YS, Yao GX, Wang XL, et al. A comprehensive analysis of metabolomics and transcriptomics reveals new biomarkers and mechanistic insights on DEHP exposures in MCF-7 cells. *Chemosphere*. 2020;255:126865. doi:10.1016/j.chemosphere.2020.126865
70. Lan Z, Chai K, Jiang Y, Liu X. Characterization of urinary biomarkers and their relevant mechanisms of zoledronate-induced nephrotoxicity using rats and HK-2 cells. *Hum Exp Toxicol*. 2019;38(5):598–609. doi:10.1177/0960327119829527
71. Bo L, Liu Y, Jia S, et al. Metabonomics analysis of quercetin against the nephrotoxicity of acrylamide in rats. *Food Funct*. 2018;9(11):5965–5974. doi:10.1039/c8fo00902c
72. W REN, J YIN, W GAO, et al. Metabolomics study of metabolic variations in enterotoxigenic Escherichia coli-infected piglets. *RSC Adv*. 2015;5 (73):59550–59555. doi:10.1039/c5ra09513a
73. Zhu ZX, Jiang DL, Li BJ, et al. Differential transcriptomic and metabolomic responses in the liver of nile tilapia (Oreochromis niloticus) exposed to acute ammonia. *Mar Biotechnol*. 2019;21(4):488–502. doi:10.1007/s10126-019-09897-8
74. Zhou Y, Liu H, Zhang M. Analysis of the metabolic pathways affected by hot-humid or dry climate based on fecal metabolomics coupled with serum metabolic changes in broiler chickens. *Poult Sci*. 2020;99(11):5526–5546. doi:10.1016/j.psj.2020.07.039
75. Zhang R, Zhu W, Jiang L, Mao S. Comparative metabolome analysis of ruminal changes in Holstein dairy cows fed low- or high-concentrate diets. *Metabolomics*. 2017;13(6):74. doi:10.1007/s11306-017-1204-0
76. Gao X, Guo M, Li Q, et al. Plasma metabolomic profiling to reveal antipyretic mechanism of Shuang-huang-lian injection on yeast-induced pyrexia rats. *PLoS One*. 2014;9(6):e100017. doi:10.1371/journal.pone.0100017
77. Pillai NR, Amin H, Gijavanekar C, et al. Hematologic presentation and the role of untargeted metabolomics analysis in monitoring treatment for riboflavin transporter deficiency. *Am J Med Genet A*. 2020;182(11):2781–2787. doi:10.1002/ajmg.a.61851
78. Huang X, Zhao X, Zhang X, Wang P, Zhu K, Shao B. Chlorinated disinfection byproducts of diazepam perturb cell metabolism and induce behavioral toxicity in zebrafish larvae. *Ecotoxicol Environ Saf*. 2021;220:112416. doi:10.1016/j.ecoenv.2021.112416
79. Ciappio ED, Krausz KW, Rochman M, et al. Metabolomics reveals a role for the chromatin-binding protein HMGN5 in glutathione metabolism. *PLoS One*. 2014;9(1):e84583. doi:10.1371/journal.pone.0084583